A&A, 709, A237 (2026)
https://doi.org/10.1051/0004-6361/202558839

Astronomy & Astrophysics

MICONIC: JWST/MIRI-MRS reveals heavily reprocessed polycyclic aromatic hydrocarbons in the circumnuclear disc of Centaurus A

L. Pantoni[1,⋆], M. Baes[1], L. Decin[2], P. Guillard[3,4], A. Alonso Herrero[5], L. Hermosa Muñoz[5], L. Evangelista[3], I. García-Bernete[5,14], F. Donnan[15], V. Buiten[10], S. Garcia-Burillo[9], G. Wright[8], L. Colina, T. Böker[7], G. Östlin[17], D. Dicken[8], A. Labiano[6], D. Rouan[18], P. van der Werf[10], A. Eckart[16], M. García-Marín[7], M. Güdel[11,12], Th. Henning[19], P.-O. Lagage[13], F. Walter[19], and M. J. Ward[20]

(Affiliations can be found after the references)

Received 31 December 2025 / Accepted 23 March 2026

ABSTRACT

Context. Polycyclic aromatic hydrocarbons (PAHs) constitute essential components of dust in galaxies and have a fundamental role in the physics of the interstellar medium (ISM). The impact of AGN feedback on these molecules is still under debate.

Aims. We aim to present a detailed analysis of the spatially resolved properties of PAHs in the central 7″ × 12″ (∼100 × 200 pc^2) of Centaurus A (Cen A). We used the JWST/MIRI-MRS observations at $\lambda \sim 5 - 28$ μm taken as part of the MIRI European consortium's Guaranteed Time Observation (GTO) program MICONIC, with angular resolution between 0.35″ and 1″ (∼6−17 pc).

Methods. We derived PAH moment-zero maps through local continuum subtraction and extracted one-dimensional spectra in five regions of interest, including the nucleus, the circumnuclear disc, and a region characterised by a prominent deficiency in PAH emission. We decomposed the spectra into continuum, emission lines, and PAHs, from which we extracted PAH intensities and equivalent widths (EWs).

Results. Polycyclic aromatic hydrocarbon emission is predominantly distributed in a ring-like structure with localised intensity enhancements, at a radius of ∼40 pc from the active nucleus. Towards the north-west we observe a distinct PAH-deficient area, roughly perpendicular to the jet axis and coincident with enhanced ionised-gas velocity dispersion as well as inflowing warm and cold molecular streamers. The PAH 11.3/7.7 μm and 6.2/7.7 μm intensity ratios exceed model predictions for peri-condensed PAHs, suggesting heavily reprocessed populations characterised by more open and irregular molecular structures. PAH 11.3/12.7 μm ratios point to a prevalence of solo over duo or trio hydrogen sites, consistent with a non-negligible degree of dehydrogenation, particularly within the PAH-deficient region, where shock-driven erosion may play a major role. We measured the largest EWs in the PAH ring, whereas reduced values in the PAH-deficient region likely reflect partial destruction by shocks; in the nucleus, the small EWs are largely attributable to continuum dilution.

Key words. galaxies: active – galaxies: evolution – galaxies: ISM – galaxies: individual: Centaurus A – galaxies: nuclei – galaxies: Seyfert

1. Introduction

Polycyclic aromatic hydrocarbons (PAHs) are compact, planar, carbon-based molecules composed of fused aromatic rings and typically contain between 20 and 500 carbon atoms (up to a few nanometres in size). These molecules are primarily excited by ultraviolet (UV) photons and subsequently emit in the mid-infrared (MIR) through vibrational relaxation (e.g. Allamandola et al. 1989; Peeters et al. 2021).

Polycyclic aromatic hydrocarbons are widely considered the primary carriers of the aromatic infrared bands (AIBs)[1], a set of prominent MIR emission features between 3 and 20 μm (e.g. Leger & Puget 1984; Allamandola et al. 1985; Verstraete et al. 2001; Sellgren et al. 2010; Hansen et al. 2022). Initially detected with ground-based telescopes (Gillett et al. 1973), AIBs were later observed with space-borne facilities such as ISO (e.g. Rigopoulou et al. 1999; Verstraete et al. 2001) and *Spitzer* (e.g. Werner et al. 2004; Sellgren et al. 2007) and are now known to be ubiquitous across the Universe, with detections out to a redshift of $z \sim 4$ (Riechers et al. 2014; Spilker et al. 2023).

Polycyclic aromatic hydrocarbons play a crucial role in the physics of the interstellar medium (ISM; see Tielens 2008, for a review). They contribute significantly to the photoelectric heating and the ionisation balance of the ISM (e.g. Bakes & Tielens 1994; Berné et al. 2022) and act as catalysts in the process of forming molecular hydrogen (e.g. Mennella et al. 2012; Thrower et al. 2012; Skov et al. 2014; Jones & Habart 2015; Barrera et al. 2023). They contain $\lesssim$10−15% of the interstellar carbon (e.g. Li & Draine 2001; Zubko et al. 2004; Draine & Li 2007; Jones et al. 2017; Tielens 2021), are responsible for the UV dust extinction (Weingartner & Draine 2001), and can account for up to 20% of the total infrared (IR) luminosity of star-forming, metal-rich galaxies (e.g. Smith et al. 2007). As such, PAHs serve as indirect tracers of obscured star formation (e.g. Farrah et al. 2007; Calzetti 2011; Kim et al. 2024; Ujjwal et al. 2024), although the relation may vary depending on the SFR of the system (Mordini et al. 2021; Robinson et al. 2026). Extensive observations with ISO and *Spitzer*, and more recently with JWST, revealed substantial variations in PAH emission across a wide range of Galactic and extragalactic environments, including protoplanetary discs, photodissociation regions (PDRs), HII regions, early-type galaxies, active galactic nuclei (AGNs), and low-metallicity systems (see Peeters et al. 2002; Galliano et al. 2008; Smith et al. 2007; García-Bernete et al.

⋆ Corresponding author: lara.pantoni@ugent.be

[1] Other proposed carriers include, for example, amorphous hydrogenated carbon (a-C:H; Jones et al. 2013). For simplicity, we use PAHs to refer collectively to a broader family of carbonaceous species carrying both the 2175 Å extinction bump and the AIBs.

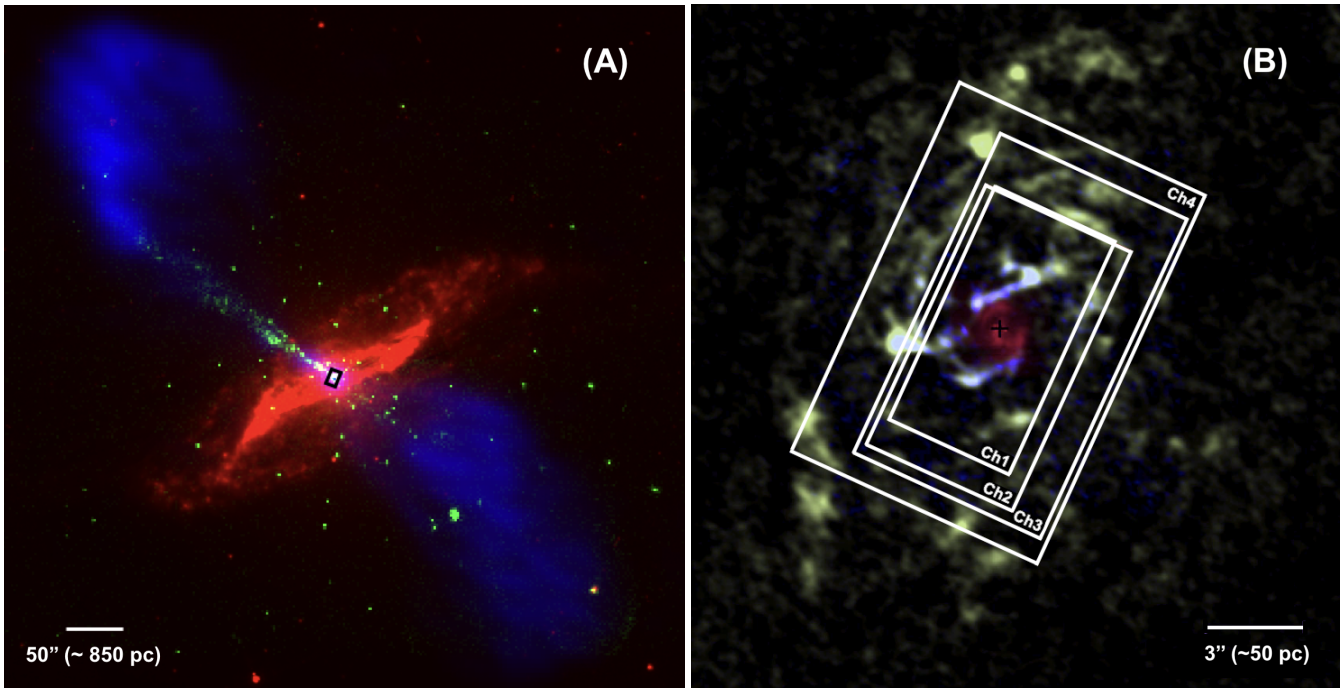

Fig. 1. Panel A: RGB composite image of Cen A. Red shows the 5.8 μm emission from Cen A as observed by *Spitzer*/IRAC (Quillen et al. 2006b,a); green corresponds to X-ray emission observed with *Chandra*/ACIS (Hardcastle et al. 2007); and blue traces the radio-jet structure imaged with the VLA (Hardcastle et al. 2003). In black we show the footprint of MIRI-MRS observations. Panel B: Zoomed-in view of the central few hundred parsecs of Cen A, showing cold molecular gas traced by CO(6–5) and CO(3–2) in blue and green and the VLT/SINFONI H_2 1-0 S(1) intensity map by Neumayer et al. (2007) in red (adapted from Espada et al. 2017). White rectangles mark the each MIRI-MRS mosaic (1 × 2 FoV). North is up and east is to the left.

2022b; Chastenet et al. 2023a,b; Sandstrom et al. 2023; Rigopoulou et al. 2024; Zhang et al. 2025; and Li 2020 for a review).

Both observational and theoretical studies have demonstrated that the relative strengths of PAH bands, particularly those in the 6−9 μm range relative to the 11.3 μm feature, serve as effective diagnostics of the local physical conditions in the ISM (e.g. Galliano et al. 2008; O'Dowd et al. 2009; Sales et al. 2010; Rigopoulou et al. 2021; García-Bernete et al. 2022b; Rigopoulou et al. 2024). In the harsh environments surrounding AGNs, especially in Seyfert nuclei, the 6−9 μm PAH bands are frequently found to be significantly suppressed compared to star-forming regions, whereas the 11.3 μm feature typically remains comparatively strong (e.g. Smith et al. 2007; García-Bernete et al. 2022b,a, 2024; Zhang & Ho 2023; Zhang et al. 2024). The suppression of the 6−9 μm features is commonly attributed to the preferential destruction of small, ionised PAH molecules and to significant structural modifications of PAHs, while large and neutral species are more likely to survive. These effects are generally interpreted as the consequence of shocks or of the hard radiation fields associated with AGNs (e.g. Diamond-Stanic & Rieke 2010; Sales et al. 2010; Zhang et al. 2022; Li 2020). Reduced PAH equivalent widths (EWs) observed in the immediate vicinity of AGNs, often interpreted as evidence of PAH destruction, may also largely result from dilution by the strong AGN MIR continuum (e.g. Desai et al. 2007; Alonso-Herrero et al. 2014; García-Bernete et al. 2015; Ramos Almeida et al. 2023).

This work presents the first sub-arcsecond, spatially resolved analysis of all major PAH emission features at $\lambda > 4.9$ μm in the innermost circumnuclear disc (ICND; central ~100 × 200 pc^2) of Centaurus A (NGC 5128; hereafter Cen A), based on JWST/MIRI-MRS observations (see footprints in Fig. 1). Cen A is the nearest active radio galaxy (D_L = 3.5 Mpc, 1″ ~ 17 pc; Neumayer et al. 2007, and $z = 0.001825 \pm 0.000017$; Baer-Way et al. 2024), making it an ideal laboratory for resolving AGN-related processes on scales of a few parsecs. Its nuclear activity is thought to be triggered by a major merger between an elliptical and a spiral galaxy (Israel 1998), which also explains the 500 pc expanding shell detected in the MIR (Quillen et al. 2006a, 2008). Optical and UV images of Cen A show a thick dust lane crossing the centre of the galaxy (e.g. Marconi et al. 2000), while MIR images reveal the presence of a dusty warped disc with a peculiar parallelogram structure (Fig. 1A, in red; see also Quillen et al. 2006b). Classified as a Type 2 Seyfert (Israel 1998), Cen A hosts a moderate-luminosity AGN (L_{bol} ~ 1−4 × 10^{43} erg s^{-1}; Beckmann et al. 2011) embedded within a complex, multi-phase circumnuclear environment that is partially shaped by AGN-powered jet and outflows (e.g. Espada et al. 2009, 2010; Borkar et al. 2021; McCoy et al. 2017; Alonso Herrero et al. 2025). In the central region of Cen A the jet (seen both in radio and in X-ray; Fig. 1A) has a position angle of 51 deg, a present-day power of $\gtrsim 10^{43}$ erg s^{-1} (e.g. Neff et al. 2015), and shows apparent subluminal motions (Clarke et al. 1992; Hardcastle et al. 2003). It appears to be nearly perpendicular to the circumnuclear molecular disc detected in CO, extending up to ~400 pc from the central cavity (see Fig. 1B; Espada et al. 2017).

Our main goal is to investigate how the AGN and shocks driven by nuclear activity affect the properties of PAHs within the ICND of Cen A, down to spatial scales of ~10 pc (~0.6″). This spatial resolution, comparable to the outer radius of AGN tori, allowed us to disentangle nuclear and circumnuclear emission, whereas previous studies of nearby AGNs, limited to ~100

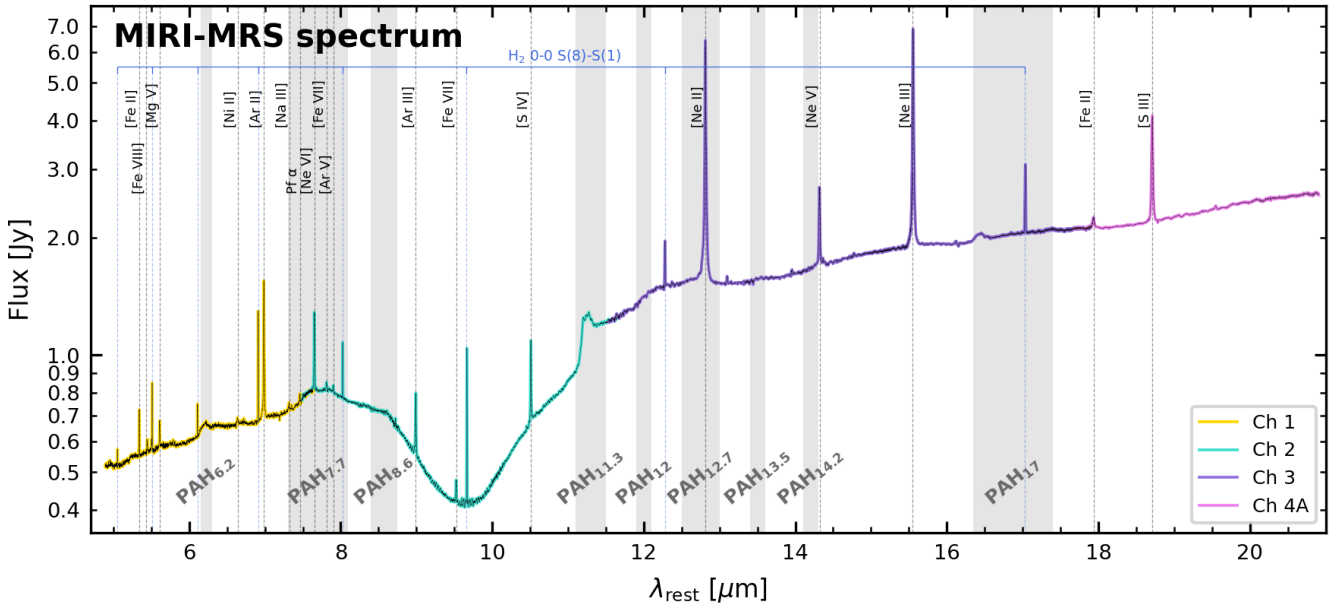

Fig. 2. MIRI-MRS spectrum of the central 7.2″ × 3.6″ region of Cen A, integrated over the Ch 1A mosaic, shown up to $\lambda_{\rm rest}$ = 21 μm. The four MRS channels are colour-coded as follows: yellow (Ch 1), cyan (Ch 2), violet (Ch 3), and pink (Ch 4). PAH features commonly observed in galactic and extragalactic environments are highlighted in grey. Ionised gas emission lines and warm molecular hydrogen transitions are marked in black and blue, respectively. A strong silicate absorption feature is evident at 9.8 μm.

pc scales, probed blended components (see also Lai et al. 2023; Zhang & Ho 2023; García-Bernete et al. 2024).

The observations with JWST/MIRI-MRS were conducted as part of the MIRI European Consortium GTO Mid-Infrared Characterization Of Nearby Iconic galaxy Centres (MICONIC) programme. Two companion studies based on MIRI-MRS observations of Cen A investigated the distribution, temperature, and excitation of warm molecular hydrogen (Evangelista et al. 2026) and the kinematics of the warm and ionised gas (Alonso Herrero et al. 2025). Along with Cen A, the MICONIC program targets several nearby, well-studied galaxies with diverse nuclear environments, including Mrk 231 (Alonso Herrero et al. 2024), Arp 220 (Buiten et al. 2025, van der Werf et al. in prep.), NGC 6240 (Hermosa Muñoz et al. 2025), SBS 0335−052 (Bik et al. in prep.), and the central region surrounding Sgr A*.

The paper is organised as follows. Section 2 describes the JWST/MIRI-MRS observations and the data reduction and homogenisation across the MRS channels. Section 3 outlines the methods used to extract the PAH emission from the MIRI-MRS cubes. In Sect. 4 we present spatially resolved maps of the main PAH features and the corresponding intensity ratios measured in selected regions of the mosaic, which we interpret in the context of recent PAH models. Section 5 discusses the impact of AGN-driven shocks on the PAH population and explores plausible evolutionary pathways. Finally, Sect. 6 summarises our conclusions.

2. Data

2.1. MIRI-MRS observations

This study is based on MIRI-MRS observations obtained as part of JWST Cycle 1's GTO programme ID 1269. The data cover the full MRS spectral range of 4.9–27.9 μm and consist of a 1 × 2 mosaic centred on the nucleus of Cen A. The spatial coverage of the mosaic (see footprints in Fig. 1) spans approximately 7″ × 12″, corresponding to a physical scale of ∼100 × 200 pc^2.

MIRI-MRS comprises four integral field units (IFUs; hereafter referred to as channels or Ch), each with a distinct spectral coverage, spectral and spatial resolution, and field of view (FoV). Each channel comes with three different grating settings (short, medium, and long; hereafter referred to as bands A, B, and C) covering adjacent wavelength ranges. The angular resolution varies from 0.35″ in Ch 1A (λ = 4.90 − 5.74 μm) to 1″ in Ch 4C (λ = 24.4 − 27.9 μm), corresponding to physical scales of approximately 6 − 17 pc at the distance of Cen A (Argyriou et al. 2023). This resolution enabled us to resolve the complex interplay between AGN activity and PAH emission in Cen A on spatial scales that were previously inaccessible. The spectral resolving power also varies across channels, with $R = \lambda/\Delta\lambda \sim$ 3700 in Ch 1 and ∼1300 in Ch 4 (Labiano et al. 2021). The FoV (1 pointing) increases with wavelength, ranging from the compact coverage of Ch 1 (3.2″×3.7″; Fig. 1B) to the nearly quadrupled area of Ch 4 (6.6″ × 7.7″).

Observations employed the four-point dither pattern optimised for extended sources (Law et al. 2023), with ten groups per integration and five integrations per exposure, in FASTR1 readout mode. The full MRS spectral range was covered in three exposures (one per band), yielding 600 seconds of on-source integration time per setting. Free-of-source background observations were obtained west of the galaxy using a two-point extended source dither pattern with identical exposure settings.

2.2. Data reduction

We reduced the MRS data using the JWST Science Calibration Pipeline v1.14.1 (Bushouse et al. 2024), within the context of 1240 of the Calibration Reference Data System (CRDS), following standard procedures (see e.g. Álvarez-Márquez et al. 2023).

We applied detector-level corrections (Stage 1) with default parameters, except when we lowered the cosmic-ray jump

Table 1. Setting for the mom0 extraction of PAH features.

λ_{PAH} [μm]	$\Delta\lambda_{PAH}$ [μm]	$\Delta\lambda_{cont}^{blue}$ [μm]	$\Delta\lambda_{cont}^{red}$ [μm]	Other lines
6.2	6.15 – 6.3	6.13 – 6.15	6.30 – 6.31	–
7.7	7.3 – 8.1	7.2 – 7.3	8.10 – 8.15	Pf α, [Ne VI], [Fe VII], [Ar V], H_2 0-0 S(4)
8.6	8.4 – 8.75	8.38 – 8.4	8.75 – 8.77	
11.3	11.1 – 11.5	11.0 – 11.1	11.50 – 11.52	–
12.7	12.48 – 13.03	12.46 – 12.48	13.03 – 13.05	[Ne II]
16.5	16.35 – 16.65	16.2 – 16.35	16.65 – 16.8	–

Notes. In order we list the observed central wavelength of each PAH complex (λ_{PAH}), the wavelength interval used for its extraction ($\Delta\lambda_{PAH}$), the blue and red continuum windows ($\Delta\lambda_{cont}^{blue}$, $\Delta\lambda_{cont}^{red}$), and any overlapping gas-phase emission lines. PAH 16.5 μm is usually included in the 17 μm complex.

detection threshold to 3.5σ and enabled cosmic-ray shower flagging (Morrison et al. 2023). In Stage 2, we enabled 2D pixel-by-pixel background subtraction and residual fringe correction, and applied the JWST pipeline bad-pixel self-calibration, which statistically identifies outliers in the background frames, resulting in ∼0.5% of pixels being flagged (Argyriou et al. 2023; Gasman et al. 2023; Patapis et al. 2024). In Stage 3, we disabled master background subtraction and sky matching due to the introduction of artefacts (Law et al. 2023).

The final reconstructed cubes were astrometrically aligned using the MIRI imager in parallel (i.e. off-target) and registered to the *Gaia* DR3 catalogue, achieving a positional accuracy better than 0.1″. They were reoriented to standard sky coordinates (north up; east left), resulting in final mosaic areas ranging approximately from 7.5″ × 3.8″ in Ch 1 to 11.7″ × 7.2″ in Ch 4.

In Fig. 2 we present the spectrum extracted over the full Ch 1A mosaic (see Fig. 1B) covering an area of 7.2″ × 3.6″, up to λ_{rest} = 21 μm. Owing to the improved spectrophotometric calibration (Gasman et al. 2023; Law et al. 2025), no band stitching was necessary, except for a minor additive adjustment of 0.025 Jy to align Ch 1A and Ch 2A and B.

The spectrum exhibits prominent PAH emission features at 6.2, 7.7, 8.6, 11.2, 12.0, and 16.5 μm (the latter usually included in the 17 μm complex). Intrinsically fainter features at 12.7, 13.5, and 14.2 μm are more difficult to detect, given the strong MIR continuum from the AGN dusty torus. Alongside PAHs, the spectrum reveals a rich set of ionised gas emission lines and the S(1)–S(8) warm H_2 pure rotational transitions (see Alonso Herrero et al. 2025 and Evangelista et al. 2026).

3. Extraction of PAH features

To characterise the PAH features in the ICND of Cen A, we first derived their two-dimensional (2D) spatial distribution. Then, we extracted one-dimensional (1D) spectra from five regions of interest identified in the maps and measured the PAH feature fluxes and EWs. In the following, we describe the methods used for the 2D and 1D extractions and subsequent analysis.

3.1. 2D extraction

We constructed the moment-zero (mom0) maps of the most prominent PAH emission features (listed in Table 1) by locally subtracting the underlying continuum emission. Before extracting the mom0 maps, we merged the four individual channels into a single data cube (hereafter 'super-cube'), as several of the broader PAH complexes (e.g. the 7.7 μm and 11.3 μm features) straddle adjacent channels. We then resampled all data to a common spaxel scale of 0.6″ (∼10 pc; i.e. Ch 3B angular resolution, Law et al. 2023) and set the spectral sampling to $\Delta\lambda$ = 0.005 μm. We carefully inspected the resulting cube and found no evidence of artefacts introduced by the re-sampling. Relative to PAHs extracted at the native spaxel scale, the re-sampled maps exhibit a similar intensity distribution, but with an improved signal-to-noise ratio.

We modelled the underlying continuum with a linear fit over narrow wavelength intervals of ∼0.01–0.15 μm to minimise continuum variability, and selected to lie immediately adjacent to each PAH band, as reported in Table 1. Alternative choices, such as broader windows or higher order models, did not give any significant improvement. We then subtracted the fitted continuum from the super-cube and integrated the PAH flux densities within the corresponding wavelength intervals (Table 1). We caution that local continuum subtraction may partly suppress emission in the broad PAH wings that are blended with the strong MIR continuum and, thus, underestimate the total flux. For this reason, we did not use our mom0 maps to compute PAH intensity ratios.

Several PAH bands overlap with one or more emission lines from warm H_2 and ionised gas (Table 1). To minimise contamination, we excluded these lines from the integration intervals[2]. Nevertheless, we cannot fully rule out residual line contributions, which may still influence the resulting PAH mom0 maps.

3.2. 1D extraction

We extracted 1D spectra from five regions of interest: the full Ch 1A mosaic, the nucleus, the circumnuclear region (defined as the full Ch 1A mosaic minus the nuclear emission), the PAH ring, and a PAH-deficient region located perpendicular to the jet axis. A schematic representation of the extraction regions is shown in the right panel of Fig. 3, with additional details on the aperture definitions provided in Appendix B.

Since the PAH emission features are confined to wavelengths of $\lambda \leq 17$ μm, we limited our analysis to the 5–21 μm range (up to Ch 4A), which still ensures adequate sampling of the underlying continuum at longer wavelengths. This choice reduces instrumental systematics, as data at $\lambda \gtrsim 25$ μm are increasingly affected by artefacts and reduced sensitivity, rendering them unreliable for quantitative analysis. Furthermore, by excluding Ch 4B, we were able to define extraction regions large enough to avoid convolution across channels. Given the non-Gaussian

[2] The excluded wavelength window is centred on the gas emission line and set to $4 \times \Delta\lambda \sim 0.02$ μm.

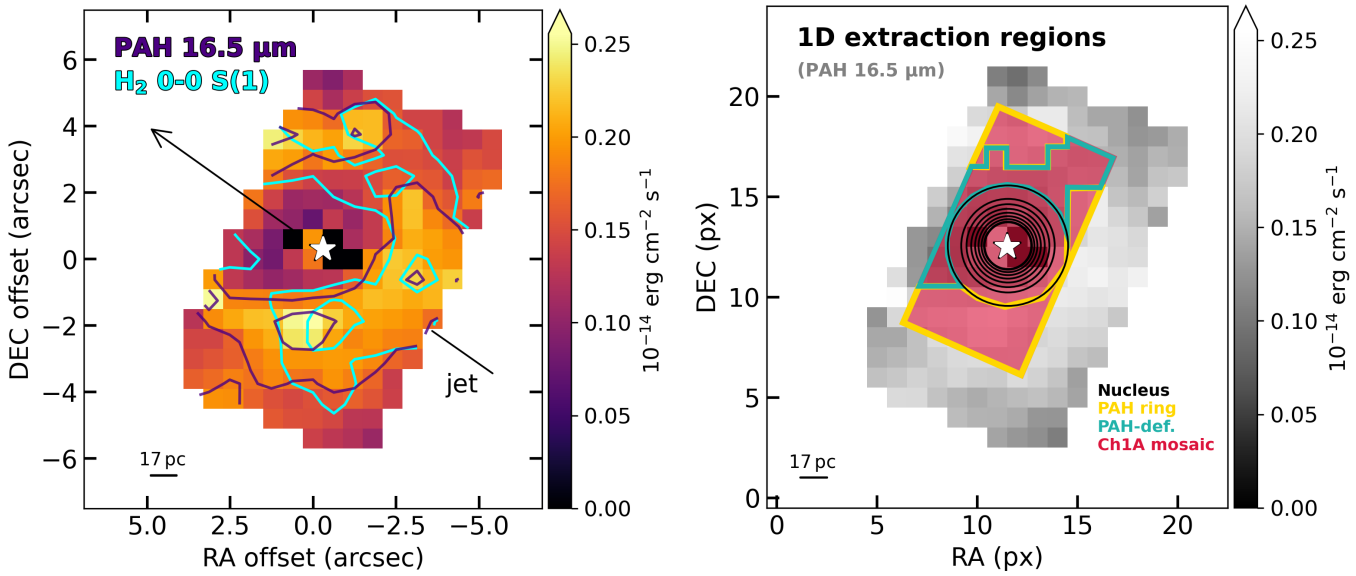

Fig. 3. Left: Mom0 map of the PAH 16.5 µm feature in the nuclear region of Cen A at 0.65″ resolution (~11 pc), obtained after subtraction of the local continuum. Violet contours show the PAH emission at levels of $(0.2, 0.25) \times 10^{-14}$ erg cm^{-2} s^{-1}. Cyan contours trace the H_2 0-0 S(1) 17.03 µm rotational line at levels of $(0.19, 0.23) \times 10^{-14}$ erg cm^{-2} s^{-1}. The black arrows indicate the position angle of the jet (i.e. PA_{jet} = 51 deg). Bright pixels near the AGN position are artefacts resulting from the local continuum subtraction. Right: 1D extraction regions defined within the Ch 1A mosaic (red filled area), overlaid on the PAH 16.5 µm surface density map (grey scale): nucleus (concentric circular areas in black), PAH ring (yellow), PAH-deficient region (green). The circumnuclear region is defined as the full Ch 1A mosaic minus the nuclear emission. In both panels, the star marks the peak of the continuum, corresponding to the position of the AGN. The [0,0] point on the axes (pixel [11,12]) denotes the centre of the sub-channel array (Ch 3C). North is up and east is to the left.

MIRI-MRS point-spread function and the strong diffraction features induced by the nuclear point source in Cen A, such convolution would likely introduce artefacts and bias the results. For the same reason, we did not perform a pixel-by-pixel spectral decomposition to derive the PAH mom0 maps. Instead, we adopted a local continuum subtraction approach, as described in Sect. 3.1.

3.3. 1D spectral decomposition with SPIRIT

We derived the integrated PAH fluxes and EWs using the SPectral InfraRed Inference Tool (SPIRIT[3]; Donnan et al. 2024), a spectral-decomposition framework adapted for application to JWST IFU spectroscopy. SPIRIT performs a simultaneous fit to the MIR dust continuum, PAH features, and gas emission lines, while accounting for differential extinction.

The continuum is described by a non-parametric distribution of modified blackbodies (MBBs; $T = 35 - 1500$ K) with wavelength-dependent emissivity from Li & Draine (2001, their Table 6) and the empirical extinction law of Donnan et al. (2023, their Appendix A). Stellar emission is included through two flexible stellar population synthesis (FSPS) templates (Conroy et al. 2009; Conroy & Gunn 2010) representing 100 Myr and 10 Gyr populations, each subject to an independent foreground extinction screen. PAH bands are modelled with Drude profiles, incorporating asymmetric components to capture the substructure revealed by MIRI-MRS (e.g. Chown et al. 2024). Emission lines are masked during the continuum and PAH fitting; their fluxes are subsequently recovered from the residual spectrum by integrating each line over its local continuum.

By incorporating differential extinction, SPIRIT recovers physically plausible dust geometries in which the hottest, most deeply embedded components suffer strong attenuation, while cooler dust remains only mildly obscured. This makes the method particularly well suited for decomposing the spectra of compact obscured nuclei (CONs), frequently found in Seyfert 2 and (ultra-)luminous infrared galaxies (ULIRGs), where the MIR continuum is often dominated by the AGN torus emission (e.g. Donnan et al. 2024; García-Bernete et al. 2024; Hermosa Muñoz et al. 2025).

[3] https://github.com/FergusDonnan/SPIRIT

4. Results

4.1. PAH spatial distribution

All PAH features display remarkably similar spatially resolved morphologies, with the exception of the 7.7 µm complex (see Figure A.1). We adopted the 16.5 µm PAH feature as our morphological reference, as it lies within MIRI-MRS Ch 3C, which offers the largest FoV and enables a direct comparison with the least energetic H_2 pure rotational line accessible with MIRI-MRS, namely the H_2 0–0 S(1) line at 17.03 µm (Fig. 3, left panel; see Appendix A for details on the H_2 mom0 extraction).

Within the ICND, the PAH emission is distributed in a ring-like structure and shows a pronounced deficit relative to the local continuum within the inner ~40 pc (in radius), corresponding to the region from which the jet is launched. However, we cannot rule out the presence of PAH features at $r < 40$ pc, which may be buried within the strong MIR continuum. The PAH emission is not spatially uniform, but instead appears clumpy, with localised intensity enhancements that are offset by several tens of parsecs from the brightest H_2 clumps. We also identified a distinct PAH-deficient region towards the north-west, oriented approximately perpendicular to the jet axis and spatially coincident with one of the brightest H_2 peaks. This region further coincides with

Table 2. PAH, warm molecular hydrogen, and ionised gas emission line intensities.

Line / feature	λ_c [μm]	Ch 1A mosaic [10^{-17} W/m^2]	Nucleus [10^{-17} W/m^2]	Circumnucl. reg. [10^{-17} W/m^2]	PAH ring [10^{-17} W/m^2]	PAH-def. reg. [10^{-17} W/m^2]
PAH	6.2	108 ± 20	8.44 ± 2.8	125 ± 15	67 ± 9	31 ± 4
PAH complex	7.7	251 ± 39	70 ± 14	268 ± 36	132 ± 17	46 ± 6
PAH complex	8.6	65 ± 18	0.12 ± 0.05	72 ± 17	47 ± 9	16 ± 5
PAH complex	11.3	473 ± 103	164 ± 45	224 ± 16	115 ± 8	42 ± 3
PAH	12	377 ± 71	370 ± 100	92 ± 8	28 ± 3	8.2 ± 0.7
PAH complex	12.7	233 ± 44	177 ± 49	97 ± 9	48 ± 4	13 ± 1
PAH complex	17	164 ± 32	57 ± 13	113 ± 9	71 ± 5	30 ± 2
H_2 0-0 S(3)	9.664	15.87 ± 0.05	1.36 ± 0.03	14.5 ± 0.06	5.09 ± 0.01	3.789 ± 0.005
H_2 0-0 S(2)	12.278	8.27 ± 0.05	0.51 ± 0.15	8.19 ± 0.05	3.39 ± 0.02	2.13 ± 0.03
H_2 0-0 S(1)	17.035	14.1 ± 0.2	2.63 ± 0.09	11.71 ± 0.02	6.11 ± 0.01	3.455 ± 0.005
[Ne II]	12.814	163.8 ± 0.06	132.62 ± 0.06	31.05 ± 0.03	7.17 ± 0.04	5.34 ± 0.02
[Ne V]	14.3217	23.4 ± 0.1	19.4 ± 0.1	4.29 ± 0.02	0.68 ± 0.02	0.857 ± 0.008
[Ne III]	15.555	124.43 ± 0.04	103.5 ± 0.1	20.609 ± 0.005	6.023 ± 0.004	5.71 ± 0.01

Notes. Intensities are derived using SPIRIT. The second column lists the central wavelength of each feature. PAH complexes include the following sub-components: 7.42, 7.55, 7.61, and 7.82 μm features (PAH 7.7); 8.50 and 8.61 μm (PAH 8.6); 11.20 and 11.26 μm (PAH 11.3); 12.60 and 12.77 μm (PAH 12.7); 16.45, 17.04, and 17.375 μm (PAH 17). We only list the lines used in this work.

Table 3. PAH EWs.

PAH λ_c [μm]	Ch 1A mosaic [nm]	Nucleus [nm]	Circumnucl. reg. [nm]	PAH ring [nm]	PAH-def. reg. [nm]
6.2	24 ± 2	2.3 ± 0.2	140 ± 10	310 ± 30	290 ± 30
7.7 complex	69 ± 7	24 ± 2	370 ± 40	700 ± 70	460 ± 50
8.6 complex	25 ± 2	0.055 ± 0.005	130 ± 10	380 ± 40	240 ± 20
11.3 complex	220 ± 20	89 ± 9	630 ± 60	1400 ± 100	910 ± 90
12	16 ± 2	190 ± 20	240 ± 20	320 ± 30	160 ± 20
12.7 complex	93 ± 9	83 ± 8	250 ± 30	500 ± 50	220 ± 20
17 complex	78 ± 8	31 ± 3	400 ± 40	1100 ± 100	790 ± 80

Notes. Same as Table 2. We assume an uncertainty of 10%.

Table 4. Intensity ratios.

PAH ratios	Ch 1A mosaic	Nucleus	Circumnucl. reg.	PAH ring	PAH-def. reg.
6.2/7.7	0.43 ± 0.04	0.12 ± 0.03	0.47 ± 0.04	0.51 ± 0.05	0.67 ± 0.05
6.2/11.3	0.23 ± 0.02	0.052 ± 0.004	0.56 ± 0.04	0.58 ± 0.04	0.74 ± 0.05
7.7/11.3	0.53 ± 0.05	0.47 ± 0.05	1.2 ± 0.1	1.15 ± 0.10	1.095 ± 0.100
11.3/6.2	4.4 ± 0.3	19 ± 1	1.8 ± 0.1	1.7 ± 0.1	1.4 ± 0.1
11.3/7.7	1.9 ± 0.2	2.3 ± 0.2	0.8 ± 0.2	0.9 ± 0.3	0.9 ± 0.3
11.3/12.7	2.0 ± 0.2	0.9 ± 0.1	2.3 ± 0.3	2.4 ± 0.3	3.2 ± 0.4
$L_{H2}/L_{PAH\,7.7}$	0.11	0.06	0.13	0.11	0.20

Notes. Same as Table 2. The quoted uncertainties are fully propagated through each ratio. H_2 luminosity (L_{H2}) is obtained as the sum of H_2 0–0 S(1), H_2 0–0 S(2), and H_2 0–0 S(3) intensities (Tab. 2).

both an area of enhanced velocity dispersion in the ionised gas (Alonso Herrero et al. 2025) and the innermost inflowing branch of molecular gas traced by CO(3–2) (Espada et al. 2017), as shown in Fig. 10.

4.2. Integrated PAH features

We fitted the five spectra extracted from the regions in Fig. 3 (right panel) with SPIRIT (Donnan et al. 2024), as described in Sect. 3.2. Fig. 4 presents the best-fitting models for the five regions together with their residuals, which remain within 10–15%. The nuclear spectrum yields the poorest fit (with $\chi^2_{red} = 30$) and shows the largest residuals, particularly across the 9–12 μm range. The intense AGN continuum makes it difficult to constrain the PAH features, which are strongly diluted. As such, the nuclear PAH intensities are possibly biased and potentially underestimated. In Appendix C we assess the effect of excluding the PAH features from the spectral fit. The goodness of fit improves markedly when the nucleus is excluded: the reduced χ^2 decreases from 12 for the full Ch 1A extraction to 3.2 for the circumnuclear region (cf. the top and third panels of Fig. 4). The PAH ring and the PAH-deficient region's spectra are reproduced

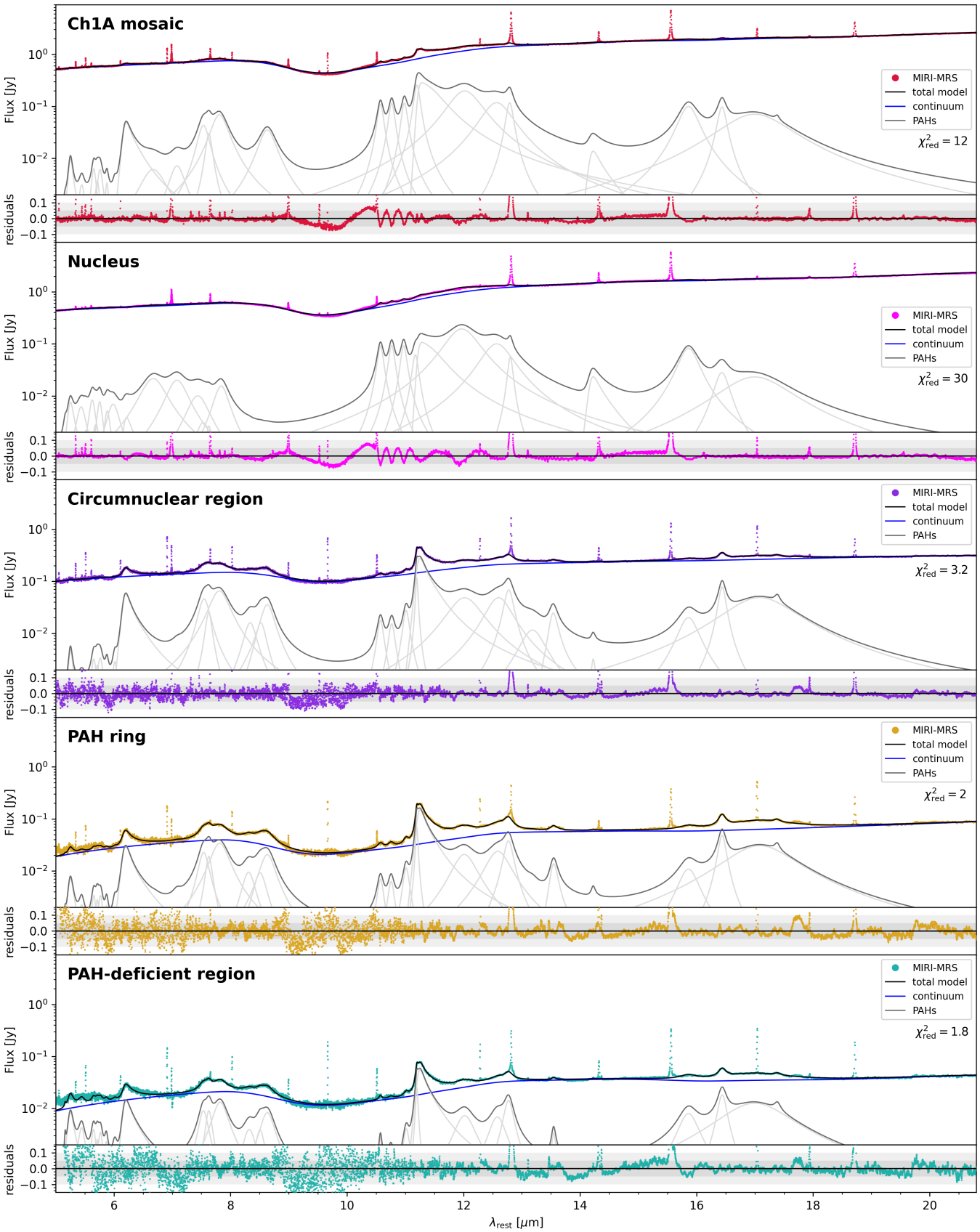

Fig. 4. MIRI-MRS spectra extracted from five regions (top to bottom): full Ch 1A mosaic (red), nucleus (magenta), circumnuclear region (violet), PAH ring (yellow), and PAH-deficient region (green). Extraction regions are shown in the right panel of Fig. 3. Black lines indicate the total best-fit models from the MIR decomposition tool (Donnan et al. 2024); blue and grey lines show the fitted continua (stellar + AGN) and PAH components, respectively. Fit residuals are displayed below each panel; the reduced χ^2 is reported below the legend.

with very high accuracy, with $\chi^2_{\rm red}$ values of 2 and 1.8, respectively.

The typical uncertainties on the integrated PAH intensities computed by SPIRIT via bootstrap re-sampling are below a few percent, reflecting the small errors reported by the JWST pipeline and likely underestimated. We therefore adopted a more realistic error estimate based on the median absolute deviation (MAD) of the PAH flux densities within each extraction region. The MAD is less sensitive to outliers and remains robust even for small samples. In Table 2 we list the PAH band intensities and other relevant spectral lines, while in Table 3 we report the PAH EWs, and in Table 4 we provide the PAH intensity ratios.

Because individual PAH bands arise from distinct vibrational modes, PAH intensity ratios provide powerful diagnostics of PAH size, charge state, and molecular structure (e.g. Draine & Li 2001; Galliano et al. 2008; Rigopoulou et al. 2021, 2024). In the following sections, we investigate the properties of PAH molecules in the ICND of Cen A by comparing the measured ratios with theoretical predictions and with results from previous studies of Seyfert nuclei.

4.2.1. PAH size and charge

Ratios between bands arising from the same vibrational modes (e.g. the C–C stretching ratio 6.2/7.7) are sensitive to the PAH size distribution, as first noted by Draine & Li (2001), and more recently confirmed by, for example, Rigopoulou et al. (2021) and Draine et al. (2021, see their Fig. 5). Ratios between the 11.3 μm C–H out-of-plane bending feature, enhanced in neutral species, and the 6–9 μm C–C stretching features, intrinsically stronger in ionised PAHs, directly trace the PAH charge state and, by extension, the physical conditions of the emitting region (Allamandola et al. 1999; Hudgins & Allamandola 1999; Hony et al. 2001; Kim & Saykally 2002; Galliano et al. 2008).

We used the 6.2/7.7 and 11.3/7.7 PAH band ratios (Table 4) to constrain the PAH size and charge in the five regions of interest. Both the 6.2 and 7.7 μm features predominantly arise from ionised PAHs, rendering their ratio relatively robust in star-forming environments but less reliable in AGN-dominated regions, where recent evidence points to a predominantly neutral PAH population (e.g. García-Bernete et al. 2024). In this context, the ratio between the 17 (or 11.3) and 3.3 μm features, emitted mainly by neutral PAHs, has been shown to provide a reliable alternative tracer of PAH size (e.g. Rigopoulou et al. 2024). That said, we are compelled to rely on the 6.2/7.7 ratio, as the MIRI-MRS data do not extend to wavelengths shorter than 4.9 μm, and the available NIRSpec observations of Cen A (Dumont et al. 2025) only cover the central $\sim 3'' \times 3''$ ($\sim 50 \times 50$ pc^2).

In Fig. 5 we compare our measurements with the theoretical grids of Rigopoulou et al. (2021) and the model predictions by Draine & Li (2001). Since theoretical models depend on the intensity of the radiation field exciting the PAH molecules, we estimated an upper limit to the AGN radiation in the centre of Cen A (Appendix E), i.e. $\sim 10^3$ ISRF, where ISRF $= 2.2 \times 10^{-5}$ W m^{-2} $= 220$ erg s^{-1} m^{-2} is the interstellar radiation field in the solar neighbourhood (Mathis et al. 1983; Galliano 2022). We restricted the theoretical predictions in Fig. 5 ($0.5–10^3$ ISRF) accordingly.

All five regions (see Table 4) lie in the upper part of the plot, at 11.3/7.7 $\geq$ 0.7. Spectral fitting performed with CAFE (Marshall et al. 2007; Diaz-Santos et al. 2025), another tool widely used for decomposing MIR spectra of AGNs (e.g. Armus et al. 2023; Lai et al. 2023), yields PAH ratios consistent with our measurements (grey filled symbols in Fig. 5), albeit with large uncertainties (see Appendix D). This agreement indicates that our results are robust against the choice of spectral decomposition method.

The nuclear region, lying in the upper left corner of the plot, is likely biased towards high 11.3 μm values, due to the combined effects of the strong 9.8 μm silicate absorption feature and the intense MIR continuum, which leads to only partial detection of the 6.2 and 7.7 μm features. Consequently, we treat the 11.3/7.7 ratio as an upper limit, while the 6.2/7.7 ratio remains poorly constrained.

The PAH ratios in the other four regions lie at 6.2/7.7 $\geq$ 0.4 and 11.3/7.7 $\geq$ 0.7. While large neutral PAHs (> 100 C atoms) could in principle produce high 11.3/7.7 ratios, they would be expected to show low 6.2/7.7 ratios, contrary to our observations. Only the PAH ring and circumnuclear region are consistent with small ($N_C \sim 20$) neutral PAHs (Rigopoulou et al. 2021), yet they are offset from the predictions by Draine & Li (2001).

The predictions of both Draine & Li (2001) and Rigopoulou et al. (2021) are based on models of peri-condensed PAHs (e.g. pyrene, coronene, and ovalene). Our ratios could be naturally explained if the PAH population were dominated by cata-condensed species (e.g. naphthalene, pentaphene, and pentacene), which have more open and irregular structures (see Li 2020 and references therein). Cata-condensed PAHs contain more H atoms per C atom than peri-condensed PAHs, resulting in intrinsically higher 11.3/7.7 ratios at a given 6.2/7.7 ratio.

Computational studies of cata-condensed PAHs (e.g. Pathak & Rastogi 2005) indicate that neutral species show enhanced C–H stretching (3.3 μm), while in cations the C–C stretch (6.2 and 7.7 μm) and C–H in-plane modes (8.6 μm) dominate. Since the PAH population in the five regions of Cen A appears to be dominated by neutral species, diagnostics based on the 6.2/7.7 ratio may bias our conclusions. Direct access to the 3.3 μm feature would provide an independent verification of our findings. Ultimately, theoretical models that incorporate cata-condensed PAH species are required to further test and confirm this scenario.

Alternatively, the extreme 11.3/7.7 ratios could result from poor PAH fitting. This is likely the case for the nucleus and the full Ch 1A mosaic, where the AGN MIR continuum dominates.

Diamond-Stanic & Rieke (2010) reported similar PAH ratios for the central regions ($3.6'' \times 7.2''$, median distance 22 Mpc) of six Seyferts (NGC 5194, NGC 4501[4], NGC 4639, NGC 1433, NGC 2639, NGC 5005), shown in Fig. 5 as filled black circles. These objects lie beyond the predictions of Draine & Li (2001), but generally agree with the neutral PAH grid of Rigopoulou et al. (2021) for $N_C \lesssim 200$, except for NGC 5194 (11.3/7.7 $\sim$ 1.09, 6.2/11.3 $\sim$ 0.41), which is also classified as LINER. The authors reported for these objects enhanced H_2 emission, which might be a signature of the presence of AGN-driven shocks that collisionally excite the H_2. In this case, shocks might play a role in setting the observed PAH ratios (for further discussion see Sect. 5.1).

In Fig. 5 we also include recent MIRI-MRS measurements of local Seyfert nuclei. These comprise nuclear and outflow regions of NGC 5728, NGC 5506, and NGC 7172 (~75–100 pc; García-Bernete et al. 2024), and the nuclear regions of NGC 6552, NGC 7319, and NGC 7469 (~142–245 pc; García-Bernete et al. 2022a), comparable in size to our Cen A mosaic. Additionally, we include three 500 pc regions

[4] Comparable ratios for NGC 4501 were found by García-Bernete et al. (2022b).

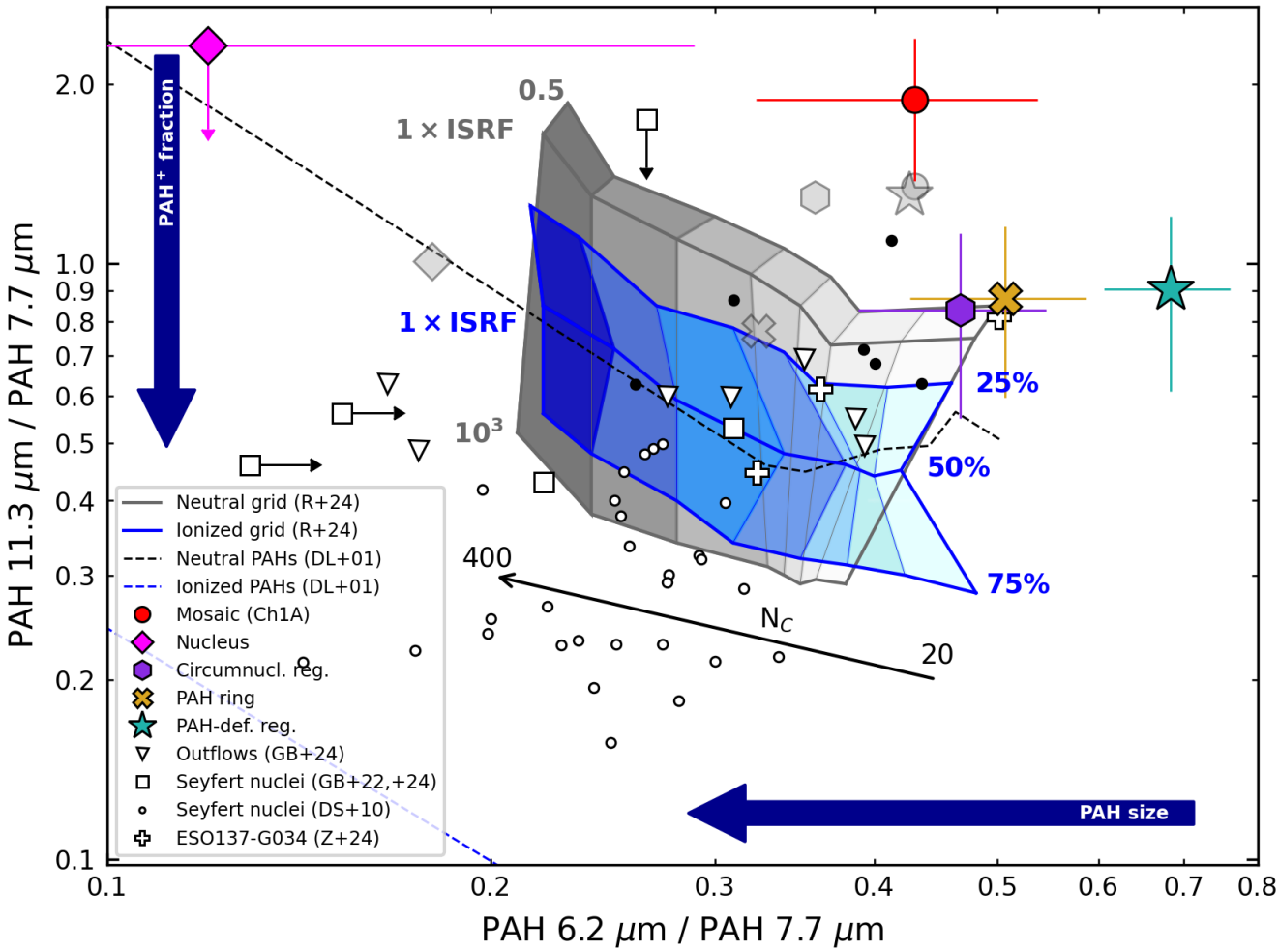

Fig. 5. PAH 11.3/7.7 μm versus PAH 6.2/7.7 μm diagnostic plot for the five regions of interest: full Ch 1A mosaic (red circle), nucleus (magenta diamond), circumnuclear region (violet hexagon), PAH ring (yellow cross), and PAH-deficient region (green star). The large uncertainty on the nuclear PAH 6.2/7.7 μm ratio and the upper limit on 11.3/7.7 μm result from partial detection of the 6.2 and 7.7 μm features (Appendix C). Grey symbols show CAFE-derived ratios (Appendix D). Uncertainties on the CAFE ratios, which span nearly the full x-range of the figure while remaining close to the SPIRIT y-axis values, were omitted for clarity. We overlay the grids of Rigopoulou et al. (2021) for neutral PAHs (grey; illuminated by 0.5−10^3 ISRF), and partially ionized PAHs (25−75%; blue; 1 ISRF). PAH size increases along the x-axis (right to left) with the number of carbon atoms (N_C) while the ionized fraction increases along the y-axis (top to bottom). The dashed black and blue curves mark the neutral and ionized PAH limits from Draine & Li (2001), for 1 ISRF. For comparison, we include PAH ratios for Seyfert nuclei from Diamond-Stanic & Rieke (2010, circles; filled symbols indicate high H_2/PAH luminosity ratios); and from García-Bernete et al. (2022a, 2024), shown as squares. Triangles denote outflow regions in the same systems. Plus symbols represent the three regions in the central kpc of the Seyfert 2 ESO 137-G034 (Zhang et al. 2024). For clarity, we omit the uncertainties associated with literature ratios.

sampling the central kiloparsec of ESO 137-G034 (Zhang et al. 2024), which are dominated by collisional shock heating.

Most of these regions lie beyond the predictions of Draine & Li (2001), but remain consistent with the neutral PAH grid of Rigopoulou et al. (2021), with ionised PAH fractions below 25%. The nuclei of NGC 5728, NGC 5506, and NGC 6652; and the outflow regions of NGC 5506 and NGC 7172, are consistent with emission dominated by large, neutral PAHs. Overall, these comparisons show that AGN-driven shocks (e.g. by nuclear outflows) preferentially destroy ionised PAHs, which is consistent with the elevated 11.3/7.7 ratios observed in the central regions of Cen A.

4.2.2. PAH hydrogenation state

PAH intensity ratios can also provide insights on the hydrogenation state of the dominant PAH species. The 11.3 μm feature is due to out-of-plane C–H bending of solo hydrogen atoms (Hony et al. 2001), while the 12.7 μm, 13.6 μm, and 14.2 μm PAH bands originate from out-of-plane bending vibrations of PAHs with duo, trio and/or quartet peripheral hydrogens (Hudgins & Allamandola 1999; Hony et al. 2001; Tielens 2008). As such, the ratio 11.3/12.7 is frequently used to infer the geometry or edge structure of interstellar PAHs. Lower 11.3/12.7 ratios imply more irregular PAHs (i.e. more duo sites), while higher 11.3/12.7 ratios point towards a dominant population of more compact PAHs (fewer duo sites).

In Fig. 6 we plot the 11.3/6.2 ratio against the 11.3/12.7 one, the latter tracing the relative contribution of duo and trio C–H groups compared to solo groups. Seyfert nuclei and outflows span a broad range of 11.3/12.7 values, although clustering at values > 1, while their 11.3/6.2 ratios range from ∼1 to ∼4. The circumnuclear regions of Cen A exhibit 11.3/12.7 ratios of $\gtrsim$ 2, consistent with those measured in Seyfert nuclei

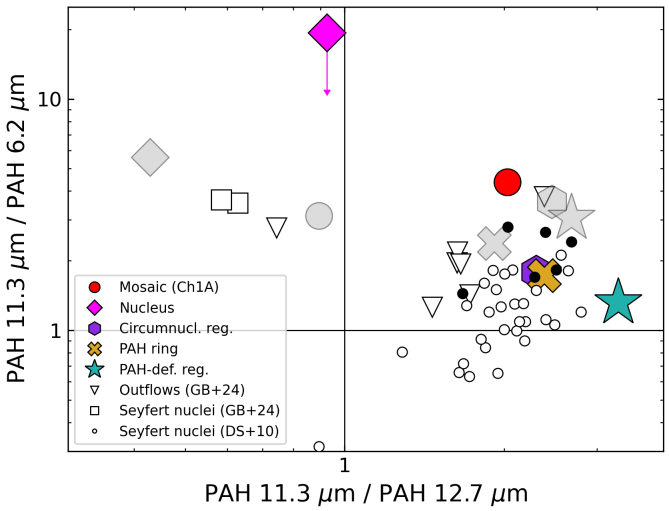

Fig. 6. PAH 11.3/6.2 μm versus PAH 11.3/12.7 μm diagnostic plot. Symbols are the same as Fig. 5. Uncertainties, between 10 – 50%, are omitted for clarity. The nuclear upper limit results from partial detection of the 6.2 μm feature (Appendix C).

(e.g. Diamond-Stanic & Rieke 2010). Such high ratios indicate a dominance of solo over duo and trio C–H groups, suggesting partial PAH dehydrogenation. This effect is strongest in Cen A's PAH-deficient region, which shows the largest 11.3/12.7 ratio.

4.2.3. PAH EWs

PAH EWs quantify the strength of PAH features relative to the local MIR continuum. They provide a useful diagnostic of PAH abundance and destruction (e.g. Roche et al. 1991; Voit 1992), though they are also strongly affected by dilution from hot-dust continuum emission (e.g. Alonso-Herrero et al. 2014; Robinson et al. 2026). As a result, PAH EWs are widely used to probe the resilience of PAHs in harsh environments, to differentiate star-forming from AGN-dominated regions (e.g. Treyer et al. 2010; García-Bernete et al. 2022b), and to trace how PAH excitation responds to variations in the intensity and hardness of the radiation field (e.g. Sales et al. 2010; Sajina et al. 2022).

The top panel of Fig. 7 shows the PAH EWs in the five regions of interest. The EWs vary substantially: they are lowest in the nucleus and in the full Ch 1A mosaic and highest in the PAH ring. The 7.7, 11.3, and 17 μm complexes exhibit the strongest variations, whereas the 12 μm feature is comparatively uniform. In the following, we focus on the 7.7 μm (primarily ionized PAHs) and 11.3 μm (primarily neutral PAHs) complexes.

In the middle panel of Fig. 7 we examine the dependence of PAH EWs on the [Ne III]/[Ne II] ratio, a standard tracer of radiation-field hardness (e.g. Thornley et al. 2000; Dale et al. 2006; Snijders et al. 2007; Pereira-Santaella et al. 2010; Inami et al. 2013). We found a pronounced decrease in both 7.7 μm and 11.3 μm EWs with increasing [Ne III]/[Ne II], consistent with previous studies (e.g. Gallimore et al. 2010; Sales et al. 2010). Two regimes are evident: (i) a steep decline for the nucleus, the Ch 1A mosaic, and the circumnuclear region; and (ii) a shallower trend for the PAH ring and the PAH-deficient region, both of which display a higher [Ne III]/[Ne II]. For the former regions, the steep decline is most naturally explained by AGN continuum dilution, consistent with their prominent MIR continua and high $\chi^2_{\rm red}$ values (see Fig. 4). However, we cannot

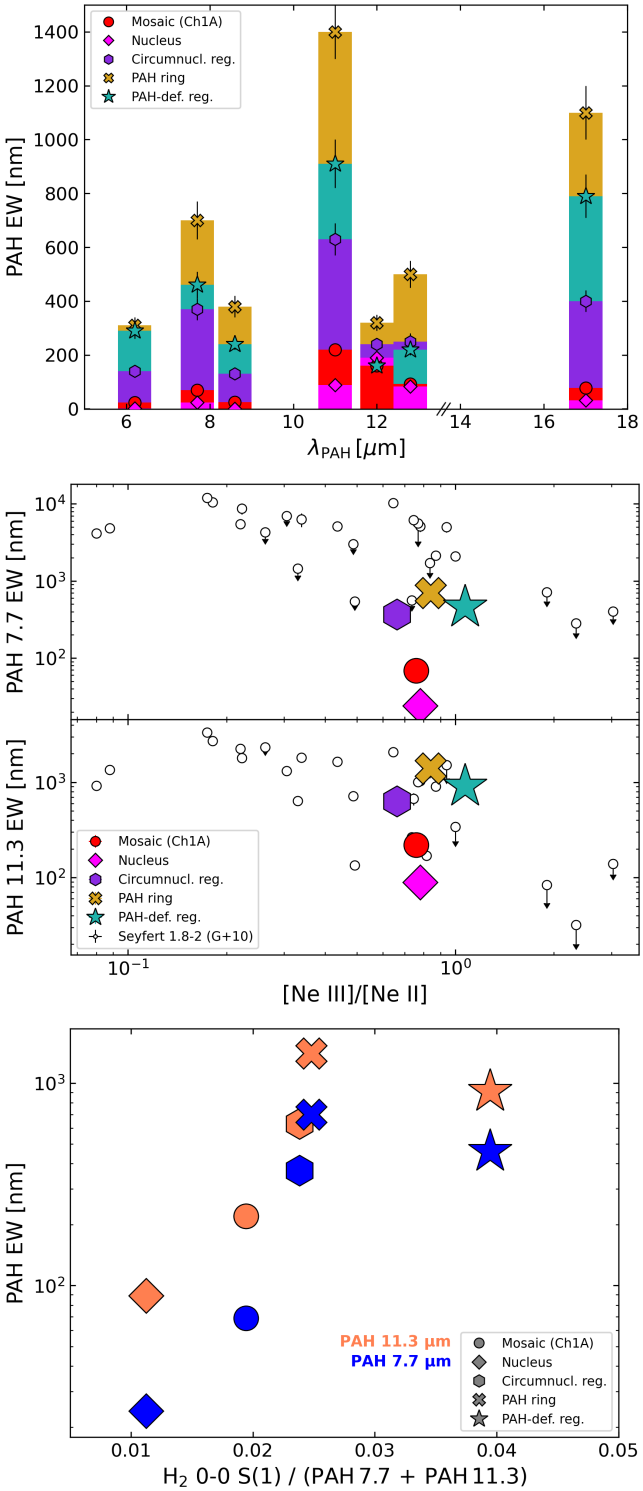

Fig. 7. Top: Bar plot of PAH EWs for the full Ch 1A mosaic (red), nucleus (magenta), circumnuclear region (violet), PAH ring (yellow), and PAH-deficient region (green). Middle: EWs of the PAH 7.7 μm (top) and 11.3 μm (bottom) complexes versus [Ne III]/[Ne II], tracing the radiation-field hardness. Points correspond to the five regions defined above, colour-coded as in the top panel. For comparison, we include Seyfert 1.8-2 nuclei from Gallimore et al. (2010) and Sales et al. (2010). Bottom: EWs of the PAH 7.7 μm (blue) and 11.3 μm (orange) complexes versus H_2 0–0 S(1) intensity relative to the PAH bands, tracing the role of shock-driven collisional excitation. Symbols denote region type: circle (Ch 1A mosaic), diamond (nucleus), hexagon (circumnuclear), cross (PAH ring), and star (PAH-deficient). EW uncertainties are smaller than or comparable to the symbol size.

exclude contribution from PAH photo-erosion by the AGN radiation field, particularly in the nucleus. The high [Ne III]/[Ne II] ratios in the PAH ring and PAH-deficient region may indicate an extra contribution from shocks to the gas excitation and ionisation (Alonso Herrero et al. 2025), as further supported by neon-line ratio diagnostics (Appendix F). Given their weaker MIR continua and low $\chi^2_{\rm red}$, continuum dilution appears negligible here and shocks are likely the dominant mechanism driving the reduced EWs in the PAH-deficient region compared to the PAH ring.

Finally, in Fig. 7 (bottom) we further investigate the influence of shocks by plotting PAH EWs as a function of the H_2 0−0 S(1) line intensity relative to PAHs (cf. Sect. 5.1). For the nucleus, the Ch 1A mosaic, and the circumnuclear region, PAH EWs increase with H_2/PAH luminosity ratio, suggesting that the steep decrease in EW with [Ne III]/[Ne II] is not shock-driven. In contrast, the PAH-deficient region shows both the highest H_2/PAH ratio and significantly reduced EWs compared to the PAH ring, reinforcing the interpretation that shocks lead to the partial destruction of both neutral and ionized PAHs in this region.

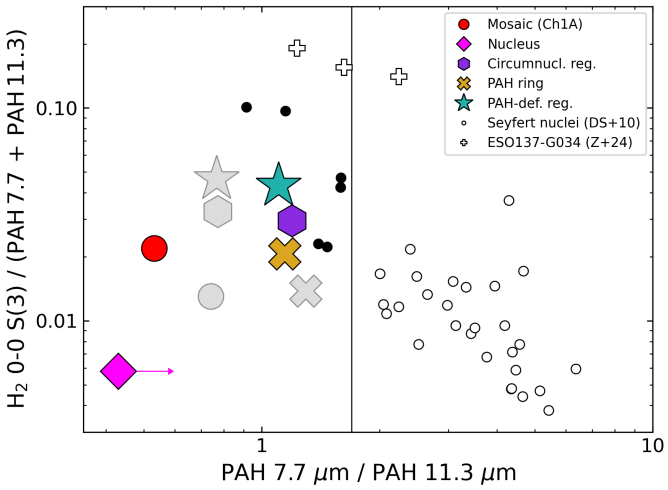

Fig. 8. H_2 0-0 S(3) intensity relative to 7.7 and 11.3 μm PAH bands diagnostic plot, quantifying shock-driven collisional excitation of H_2. Symbols are as in Fig. 5. Uncertainties, between 10−50%, are omitted for clarity. The nuclear lower limit results from partial detection of the 7.7 μm feature (Appendix C).

5. Discussion

In this section we explore the impact of AGN-driven shocks on the PAH emission features in the ICND of Cen A. Then, we assess possible evolutionary pathways of the PAH population, by combining our results with complementary sub-arcsecond-resolution observations of the molecular and ionised gases.

5.1. Impact of AGN-driven shocks

Previous studies found that collisional heating by AGN-driven shocks is associated with enhanced warm H_2 emission in the MIR (e.g. Roussel et al. 2007; Ogle et al. 2010; Guillard et al. 2012). Within the MIRI-MRS mosaic of Cen A, Evangelista et al. (2026) measured an excess in H_2 relatively to the upper limit predicted by the PDR/XDR models and required by cosmic-ray heating, which indicates that H_2 is largely collisionally excited. This is confirmed by the H_2/7.7 μm luminosity ratios (Table 4), which always exceed the threshold for the presence of a significant non-radiative heating component (i.e. $L_{\rm H2}/L_{\rm PAH\,7.7} = 0.04$; Ogle et al. 2007b, 2010; Guillard et al. 2012). Among the five regions analysed in this work, the PAH-deficient region shows the highest $L_{\rm H2}/L_{\rm PAH\,7.7}$ ratio, i.e. 0.20.

Regions with enhanced, shock-heated H_2 emission are known to exhibit systematically lower 7.7/11.3 ratios (e.g. Ogle et al. 2007a; Smith et al. 2007; Guillard et al. 2010; Vega et al. 2010). As shown in Fig. 8, the strength of the H_2 0−0 S(3) line, normalised to the 7.7 and 11.3 μm PAH features, anti-correlates with the 7.7/11.3 ratio. The five regions in Cen A's MIRI-MRS mosaic follow the same trend. Notably, they occupy the same locus as the six Seyfert nuclei from Diamond-Stanic & Rieke (2010) and the two shock-dominated regions in the central kpc of ESO 137-G034 (Zhang et al. 2024) that lie beyond the Draine & Li (2001) predictions for pericondensed PAHs (see Fig. 5).

Micelotta et al. (2010) showed that PAHs with $N_{\rm C} < 200$ experience severe structural modification in shocks of 75−100 km s^{-1} and are fully destroyed for velocities $\gtrsim$125 km s^{-1}. Although the impact of such processing on the resulting PAH band ratios remains uncertain, one plausible interpretation of the observed association between altered PAH ratios and strong H_2 emission is that shocks may leave the surviving PAHs with more open or irregular structures (i.e. cata-condensed PAHs).

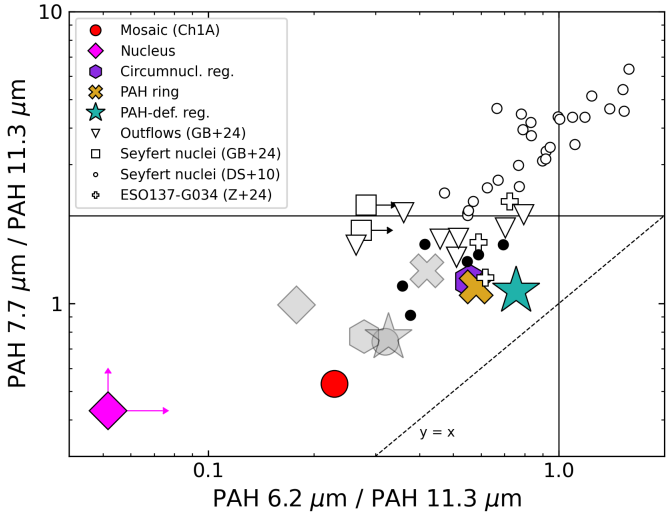

Fig. 9. PAH 7.7/11.3 μm versus PAH 6.2/11.3 μm diagnostic plot. Symbols are the same as Fig. 5. Uncertainties, between 10−40%, are omitted for clarity. The nuclear lower limits result from partial detection of the 6.2 and 7.7 μm features (Appendix C).

Notably, if collisional shocks are responsible for the observed behaviour, they appear to preferentially suppress the 6.2 and 7.7 μm features (ionised PAHs), while the 11.3 μm feature (neutral PAHs) remains the most intense. This is evident from the direct relation between 7.7/11.3 and 6.2/11.3 ratios in Fig. 9, where Seyfert nuclear regions and outflows populate the bottom-left corner at low 7.7/11.3 ($\lesssim$2) and 6.2/11.3 (<1), along with the five regions of Cen A studied in this work. This is consistent with the recent results of García-Bernete et al. (2024) and Zhang et al. (2022, 2024), which found neutral PAHs to be the most resilient in Seyfert nuclei with low/intermediate-ionisation emission lines, typical of LINERs. Overall, the 7.7/11.3 ratio varies more steeply than 6.2/11.3 (i.e. the relation is shifted from

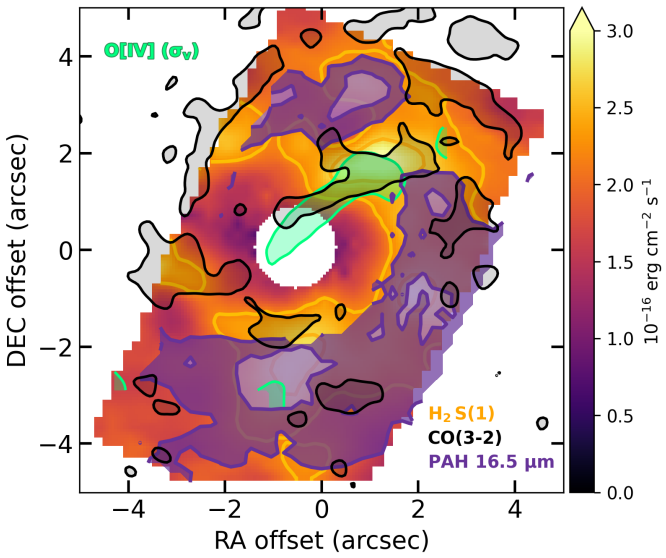

Fig. 10. Relative spatial distribution within the central ∼200 pc of warm molecular hydrogen (H_2 0−0 S(1); coloured map with yellow contours), CO(3–2) emission (black contours; Espada et al. 2017), and PAH emission (PAH 16.5 μm feature; purple-filled contours). In green, we show the [O IV] velocity dispersion from Alonso Herrero et al. (2025) for values exceeding 130 km s^{-1}. All maps were resampled to match the CO(3–2) mom0 map (Δxy = 0.35″).

the bisector to higher 7.7/11.3 values; Fig. 9), indicating stronger suppression of the 7.7 μm feature.

5.2. PAH evolutionary pathways in the centre of Cen A

The synergy between sub-arcsecond maps of PAHs, ionised gas, and cold and warm molecular gas is key to probing the spatially resolved ISM physics and the impact of AGN feedback. In Fig. 10 we present an overview of the multi-phase ISM in the ICND of Cen A. The H_2 0−0 S(1) mom0 map (see also Evangelista et al. 2026) is overlaid with the PAH 16.5 μm feature emission (see left panel of Fig. 3), the CO(3–2) line emission by Espada et al. (2017), and the velocity-dispersion map of [O IV] by Alonso Herrero et al. (2025).

The central area of the mosaic, from which the jet is launched, shows a remarkable deficiency in CO (for $r \leq$ 20−30 pc; Espada et al. 2017)[5], H_2 0−0 S(1), and PAHs ($r \leq 40$ pc). The latter are distributed on a ring-like structure, showing local regions of intensity enhancement. In the direction perpendicular to the jet, high-velocity dispersion is observed in the ionised gas phase, which is consistent with the presence of an expanding jet-inflated bubble, as predicted by hydrodynamical simulations (Alonso Herrero et al. 2025). The bubble likely interacts with the circumnuclear disc, potentially inducing gas inflows and/or outflows (Alonso Herrero et al. 2025). A pronounced deficit of PAH emission is observed in the direction of the jet-inflated bubble (Fig. 10), as well as deviations from circular motion in the molecular gas and inflow streamers (Espada et al. 2017; Alonso Herrero et al. 2025; Evangelista et al. 2026). The resulting shocks can strongly affect interstellar dust through grain-grain shattering and ion-grain sputtering (e.g. Jones et al. 1994b,a, 1996). Indeed, this region (i.e. the PAH-deficient region) shows the highest L_{H2}/L_{PAH} ratio, the most reduced PAH EWs, and the highest dehydrogenation. Although the gas within the MIRI-MRS mosaic is partly collisionally excited by shocks (Alonso Herrero et al. 2025; Evangelista et al. 2026), some of the prominent PAH emission in the ICND may arise from entrained clumps shielded by cold H_2 and not fully exposed to shocks or the hot post-shock gas (Micelotta et al. 2010), which may explain the large EWs in the PAH ring. While the column density of warm H_2 ($\sim 8 \times 10^{20}$ cm^{-2}; Evangelista et al. 2026) is too low to afford significant protection, the cold H_2 column density reported by Israel et al. (2014), i.e. $N_{H_2}^{cold} = (1.7 \pm 0.1) \times 10^{22}$ cm^{-2}, is sufficient to shield PAHs, although this value is averaged over the central 22″ (∼400 pc in diameter). Overall, PAH intensity ratios across the Cen A MIRI-MRS mosaic point to a strongly reprocessed PAH population dominated by neutral species with solo hydrogen sites, potentially exhibiting open and irregular structures.

[5] Similar evidence was found by García-Burillo et al. (2024) for a sample of 45 AGNs.

6. Summary and conclusions

We present a detailed analysis of the PAH emission in the inner 7″×12″ (∼100×200 pc^2) of Cen A, observed with JWST/MIRI-MRS as part of Cycle 1's GTO programme ID 1269. The spatial resolution across the MRS channels ranges from 0.35″ to 1″ (6−17 pc). Our study focuses on five regions of interest: the full Ch 1A mosaic, the nuclear region, the circumnuclear region (i.e. the mosaic excluding the nucleus), the PAH ring, and the PAH-deficient region. We summarise our results as follows.

- The PAH emission is mostly distributed in a ring-like structure with localized clumps, located at a radius of ∼40 pc from the AGN. A distinct PAH-deficient area is detected toward the north-west, approximately perpendicular to the jet axis.
- The 1D spectra extracted from the five regions reveal a strong AGN MIR continuum that complicates the spectral decomposition, particularly in the nucleus, where $\chi^2_{red} = 30$. Our analysis indicates that PAH emission is still present in the nuclear region, although it cannot be reliably isolated or quantified. The PAH ring and PAH-deficient regions are reproduced best by our fits, yielding $\chi^2_{red} = 2$ and 1.8, respectively.
- The PAH 11.3/7.7 μm and 6.2/7.7 μm intensity ratios we measured fall beyond model predictions by Draine & Li (2001), although the PAH ring and the circumnuclear region are consistent with the small, neutral PAHs of Rigopoulou et al. (2021). These extreme ratios can naturally be explained if the PAH population is dominated by more open and irregular species. Alternatively, they could reflect an imperfect subtraction of the underlying continuum beneath the PAH bands.
- The PAH 11.3/12.7 μm intensity ratios for the five regions indicate a dominance of solo over duo or trio hydrogen sites, consistent with previous findings for other Seyfert galaxies. The most extreme case occurs in the PAH-deficient region, where we measured the lowest 11.3/12.7 ratio.
- The lowest EWs are found in the three regions with the highest MIR continuum contribution (i.e., the nucleus, the Ch 1A mosaic, and the circumnuclear region) consistent with AGN continuum dilution. The largest EWs occur in the PAH ring, with a marked decrease in the PAH-deficient region.
- All the five regions show an $L_{H2}/L_{PAH\,7.7}$ ratio exceeding the limit set by PDR/XDR models; we find the most extreme

value in the PAH-deficient region ($L_{H2}/L_{PAH\,7.7}$ = 0.20), suggesting that the molecular gas is at least partially collisionally excited. Comparable results for the ionised gas further suggest that the ISM in the ICND of Cen A is heavily affected by AGN-driven shocks. When exposed to shocks, PAHs may experience severe structural modification, supporting the hypothesis of small, neutral, cata-condensed PAHs as the dominant PAH species in Cen A MIRI-MRS mosaics. In the most extreme cases, shocks may cause erosion or destruction of PAHs, as we claim for the PAH-deficient region, which shows both the lowest hydrogenation state and reduced EWs relative to the PAH ring. Nonetheless, the PAH-deficient region overlaps with the zone of enhanced ionised gas velocity dispersion (Alonso Herrero et al. 2025) and with inflowing warm and cold molecular streamers (Espada et al. 2017; Evangelista et al. 2026).

The synergy between sub-arcsecond-resolution maps of PAH emission, ionised gas, and cold and warm molecular gas obtained with ALMA and JWST/MIRI-MRS was crucial to get insights into the spatially resolved ISM physics and the role of AGN feedback in the central region of Cen A. Future observations with access to the 3.3 μm PAH feature will be essential to independently test and refine our interpretation of the PAH properties.

On the theoretical side, further progress will rely on extending current models to encompass a broader range of PAH species, including cata-condensed molecules, enabling a more comprehensive interpretation of PAH processing in AGN-dominated environments.

Acknowledgements. We thank the anonymous referee for the feedback and suggestions, which have helped improve this manuscript. LP acknowledges K. Matsumoto for valuable discussions. LP and MB acknowledge funding from the Belgian Science Policy Office (BELSPO) through the PRODEX project "JWST/MIRI Science exploitation" (C4000142239). AAH and LHM acknowledge support from grant PID2021-124665NB-I00 funded by MCIN/AEI/10.13039/501100011033 and by ERDF A way of making Europe. SGB acknowledges support from the Spanish grant PID2022-138560NB-I00, funded by MCIN/AEI/10.13039/501100011033/FEDER, EU.

References

Allamandola, L. J., Tielens, A. G. G. M., & Barker, J. R. 1985, ApJ, 290, L25
Allamandola, L. J., Tielens, A. G. G. M., & Barker, J. R. 1989, ApJS, 71, 733
Allamandola, L. J., Hudgins, D. M., & Sandford, S. A. 1999, ApJ, 511, L115
Alonso Herrero, A., Hermosa Muñoz, L., Labiano, A., et al. 2024, A&A, 690, A95
Alonso Herrero, A., Hermosa Muñoz, L., Labiano, A., et al. 2025, A&A, 699, A334
Alonso-Herrero, A., Ramos Almeida, C., Esquej, P., et al. 2014, MNRAS, 443, 2766
Álvarez-Márquez, J., Labiano, A., Guillard, P., et al. 2023, A&A, 672, A108
Argyriou, I., Glasse, A., Law, D. R., et al. 2023, A&A, 675, A111
Armus, L., Lai, T., U, V., et al. 2023, ApJ, 942, L37
Baer-Way, R., DeGraw, A., Zheng, W., et al. 2024, ApJ, 964, 172
Bakes, E. L. O., & Tielens, A. G. G. M. 1994, ApJ, 427, 822
Barrera, N. F., Fuentealba, P., Muñoz, F., Gómez, T., & Cárdenas, C. 2023, MNRAS, 524, 3741
Beckmann, V., Jean, P., Lubiński, P., Soldi, S., & Terrier, R. 2011, A&A, 531, A70
Berné, O., Foschino, S., Jalabert, F., & Joblin, C. 2022, A&A, 667, A159
Bohn, T., Inami, H., Togi, A., et al. 2024, ApJ, 977, 36
Borkar, A., Adhikari, T. P., Różańska, A., et al. 2021, MNRAS, 500, 3536
Buiten, V. A., van der Werf, P. P., Viti, S., et al. 2025, A&A, 699, A312
Bushouse, H., Eisenhamer, J., Dencheva, N., et al. 2024, https://doi.org/10.5281/zenodo.12556702
Calzetti, D. 2011, EAS Publ. Ser., 46, 133
Chastenet, J., Sutter, J., Sandstrom, K., et al. 2023a, ApJ, 944, L11
Chastenet, J., Sutter, J., Sandstrom, K., et al. 2023b, ApJ, 944, L12
Chastenet, J., De Looze, I., & Gordon, K. 2026, A&A, submitted
Chown, R., Sidhu, A., Peeters, E., et al. 2024, A&A, 685, A75
Clarke, D. A., Burns, J. O., & Norman, M. L. 1992, ApJ, 395, 444
Conroy, C., & Gunn, J. E. 2010, Astrophysics Source Code Library [record ascl:1010.043]
Conroy, C., Gunn, J. E., & White, M. 2009, ApJ, 699, 486
Dale, D. A., Smith, J. D. T., Armus, L., et al. 2006, ApJ, 646, 161
Desai, V., Armus, L., Spoon, H. W. W., et al. 2007, ApJ, 669, 810
Diamond-Stanic, A. M., & Rieke, G. H. 2010, ApJ, 724, 140
Diaz-Santos, T., Lai, T. S. Y., Finnerty, L., et al. 2025, Astrophysics Source Code Library [record ascl:2501.001]
Donnan, F. R., Rigopoulou, D., García-Bernete, I., et al. 2023, A&A, 669, A87
Donnan, F. R., García-Bernete, I., Rigopoulou, D., et al. 2024, MNRAS, 529, 1386
Draine, B. T., & Li, A. 2001, ApJ, 551, 807
Draine, B. T., & Li, A. 2007, ApJ, 657, 810
Draine, B. T., Li, A., Hensley, B. S., et al. 2021, ApJ, 917, 3
Dumont, A., Neumayer, N., Seth, A. C., et al. 2025, A&A, 703, A54
Espada, D., Matsushita, S., Peck, A., et al. 2009, ApJ, 695, 116
Espada, D., Peck, A. B., Matsushita, S., et al. 2010, ApJ, 720, 666
Espada, D., Matsushita, S., Miura, R. E., et al. 2017, ApJ, 843, 136
Evangelista, L., Guillard, P., & Martin, J. 2026, A&A, submitted
Farrah, D., Bernard-Salas, J., Spoon, H. W. W., et al. 2007, ApJ, 667, 149
Feltre, A., Charlot, S., & Gutkin, J. 2016, MNRAS, 456, 3354
Feltre, A., Gruppioni, C., Marchetti, L., et al. 2023, A&A, 675, A74
Galliano, F. 2022, Habilitation Thesis, 1
Galliano, F., Madden, S. C., Tielens, A. G. G. M., Peeters, E., & Jones, A. P. 2008, ApJ, 679, 310
Gallimore, J. F., Yzaguirre, A., Jakoboski, J., et al. 2010, ApJS, 187, 172
García-Bernete, I., Ramos Almeida, C., Acosta-Pulido, J. A., et al. 2015, MNRAS, 449, 1309
García-Bernete, I., Rigopoulou, D., Alonso-Herrero, A., et al. 2022a, A&A, 666, L5
García-Bernete, I., Rigopoulou, D., Alonso-Herrero, A., et al. 2022b, MNRAS, 509, 4256
García-Bernete, I., Rigopoulou, D., Donnan, F. R., et al. 2024, A&A, 691, A162
García-Burillo, S., Hicks, E. K. S., Alonso-Herrero, A., et al. 2024, A&A, 689, A347
Gasman, D., Argyriou, I., Sloan, G. C., et al. 2023, A&A, 673, A102
Gillett, F. C., Forrest, W. J., & Merrill, K. M. 1973, ApJ, 183, 87
Guillard, P., Boulanger, F., Cluver, M. E., et al. 2010, A&A, 518, A59
Guillard, P., Ogle, P. M., Emonts, B. H. C., et al. 2012, ApJ, 747, 95
Hansen, C. S., Peeters, E., Cami, J., & Schmidt, T. W. 2022, Commun. Chem., 5, 94
Hardcastle, M. J., Worrall, D. M., Kraft, R. P., et al. 2003, ApJ, 593, 169
Hardcastle, M. J., Kraft, R. P., Sivakoff, G. R., et al. 2007, ApJ, 670, L81
Hermosa Muñoz, L., Alonso-Herrero, A., Labiano, A., et al. 2025, A&A, 693, A321
Hony, S., Van Kerckhoven, C., Peeters, E., et al. 2001, A&A, 370, 1030
Hudgins, D. M., & Allamandola, L. J. 1999, ApJ, 513, L69
Inami, H., Armus, L., Charmandaris, V., et al. 2013, ApJ, 777, 156
Israel, F. P. 1998, A&ARv, 8, 237
Israel, F. P., Güsten, R., Meijerink, R., et al. 2014, A&A, 562, A96
Jensen, J. J., Hönig, S. F., Rakshit, S., et al. 2017, MNRAS, 470, 3071
Jones, A. P., & Habart, E. 2015, A&A, 581, A92
Jones, A. P., Tielens, A. G. G. M., Hollenbach, D. J., & McKee, C. F. 1994a, ApJ, 433, 797
Jones, A. P., Tielens, A. G. G. M., Hollenbach, D. J., & McKee, C. F. 1994b, Am. Astron. Soc. Meeting Abstr., 185, 26.05
Jones, A. P., Tielens, A. G. G. M., & Hollenbach, D. J. 1996, ApJ, 469, 740
Jones, A. P., Fanciullo, L., Köhler, M., et al. 2013, A&A, 558, A62
Jones, A. P., Köhler, M., Ysard, N., Bocchio, M., & Verstraete, L. 2017, A&A, 602, A46
Kim, H.-S., & Saykally, R. J. 2002, ApJS, 143, 455
Kim, H. K., Malkan, M. A., Takagi, T., et al. 2024, ApJ, 974, 253
Labiano, A., Argyriou, I., Álvarez-Márquez, J., et al. 2021, A&A, 656, A57
Lai, T.S.Y., Armus, L., U, V., et al. 2022, ApJ, 941, L36
Lai, T. S. Y., Armus, L., Bianchin, M., et al. 2023, ApJ, 957, L26
Law, D. R., Morrison, E.Jr, Argyriou, I., et al. 2023, AJ, 166, 45
Law, D. R., Argyriou, I., Gordon, K. D., et al. 2025, AJ, 169, 67
Leger, A., & Puget, J. L. 1984, A&A, 137, L5
Li, A. 2020, Nat. Astron., 4, 339
Li, A., & Draine, B. T. 2001, ApJ, 554, 778
Maragkoudakis, A., Boersma, C., Temi, P., et al. 2025, ApJ, 979, 90
Marconi, A., Schreier, E. J., Koekemoer, A., et al. 2000, ApJ, 528, 276
Marshall, J. A., Herter, T. L., Armus, L., et al. 2007, ApJ, 670, 129
Mathis, J. S., Mezger, P. G., & Panagia, N. 1983, A&A, 128, 212
McCoy, M., Ott, J., Meier, D. S., et al. 2017, ApJ, 851, 76
Mennella, V., Hornekær, L., Thrower, J., & Accolla, M. 2012, ApJ, 745, L2

Micelotta, E. R., Jones, A. P., & Tielens, A. G. G. M. 2010, A&A, 510, A36
Mordini, S., Spinoglio, L., & Fernández-Ontiveros, J. A. 2021, A&A, 653, A36
Morrison, J. E., Dicken, D., Argyriou, I., et al. 2023, PASP, 135, 075004
Neff, S. G., Eilek, J. A., & Owen, F. N. 2015, ApJ, 802, 87
Neumayer, N., Cappellari, M., Reunanen, J., et al. 2007, ApJ, 671, 1329
O'Dowd, M. J., Schiminovich, D., Johnson, B. D., et al. 2009, ApJ, 705, 885
Ogle, P., Antonucci, R., Appleton, P. N., & Whysong, D. 2007a, ApJ, 668, 699
Ogle, P. M., Antonucci, R., Appleton, P. N., et al. 2007b, Am. Astron. Soc. Meeting Abstr., 211, 97.21
Ogle, P., Boulanger, F., Guillard, P., et al. 2010, ApJ, 724, 1193
Patapis, P., Argyriou, I., Law, D. R., et al. 2024, A&A, 682, A53
Pathak, A., & Rastogi, S. 2005, Chem. Phys., 313, 133
Peeters, E., Hony, S., Van Kerckhoven, C., et al. 2002, A&A, 390, 1089
Peeters, E., Mackie, C., Candian, A., & Tielens, A. G. G. M. 2021, Accounts Chem. Res., 54, 1921
Pereira-Santaella, M., Diamond-Stanic, A. M., Alonso-Herrero, A., & Rieke, G. H. 2010, ApJ, 725, 2270
Quillen, A. C., Bland-Hawthorn, J., Brookes, M. H., et al. 2006a, ApJ, 641, L29
Quillen, A. C., Brookes, M. H., Keene, J., et al. 2006b, ApJ, 645, 1092
Quillen, A. C., Bland-Hawthorn, J., Green, J. D., et al. 2008, MNRAS, 384, 1469
Ramos Almeida, C., Esparza-Arredondo, D., González-Martín, O., et al. 2023, A&A, 669, L5
Riechers, D. A., Pope, A., Daddi, E., et al. 2014, ApJ, 786, 31
Rigopoulou, D., Spoon, H. W. W., Genzel, R., et al. 1999, AJ, 118, 2625
Rigopoulou, D., Barale, M., Clary, D. C., et al. 2021, MNRAS, 504, 5287
Rigopoulou, D., Donnan, F. R., García-Bernete, I., et al. 2024, MNRAS, 532, 1598
Robinson, L., Farrah, D., Efstathiou, A., et al. 2026, ArXiv e-prints [arXiv:2601.09810]
Roche, P. F., Aitken, D. K., Smith, C. H., & Ward, M. J. 1991, MNRAS, 248, 606
Rothschild, R. E., Markowitz, A., Rivers, E., et al. 2011, ApJ, 733, 23
Roussel, H., Helou, G., Hollenbach, D. J., et al. 2007, ApJ, 669, 959
Sajina, A., Lacy, M., & Pope, A. 2022, Universe, 8, 356
Sales, D. A., Pastoriza, M. G., & Riffel, R. 2010, ApJ, 725, 605
Sandstrom, K. M., Chastenet, J., Sutter, J., et al. 2023, ApJ, 944, L7
Sellgren, K., Uchida, K. I., & Werner, M. W. 2007, ApJ, 659, 1338
Sellgren, K., Werner, M. W., Ingalls, J. G., et al. 2010, ApJ, 722, L54
Skov, A. L., Thrower, J. D., & Hornekær, L. 2014, Faraday Discussions, 168, 223
Smith, J. D. T., Draine, B. T., Dale, D. A., et al. 2007, ApJ, 656, 770
Snijders, L., Kewley, L. J., & van der Werf, P. P. 2007, ApJ, 669, 269
Spilker, J. S., Phadke, K. A., Aravena, M., et al. 2023, Nature, 618, 708
Thornley, M. D., Förster Schreiber, N. M., Lutz, D., et al. 2000, ApJ, 539, 641
Thrower, J. D., Jørgensen, B., Friis, E. E., et al. 2012, ApJ, 752, 3
Tielens, A. G. G. M. 2008, ARA&A, 46, 289
Tielens, A. 2021, Molecular Astrophysics (Cambridge University Press)
Treyer, M., Johnson, B., Schiminovich, D., & O'Dowd, M. 2010, ArXiv e-prints [arXiv:1005.1316]
U, V., Lai, T., Bianchin, M., et al. 2022, ApJ, 940, L5
Ujjwal, K., Kartha, S. S., Akhil, K. R., et al. 2024, A&A, 684, A71
Van De Putte, D., Peeters, E., Gordon, K. D., et al. 2025, A&A, 701, A111
Vega, O., Bressan, A., Panuzzo, P., et al. 2010, ApJ, 721, 1090
Verstraete, L., Pech, C., Moutou, C., et al. 2001, A&A, 372, 981
Voit, G. M. 1992, MNRAS, 258, 841
Weingartner, J. C., & Draine, B. T. 2001, ApJ, 548, 296
Werner, M. W., Uchida, K. I., Sellgren, K., et al. 2004, ApJS, 154, 309
Zhang, L., & Ho, L. C. 2023, ApJ, 953, L9
Zhang, L., Ho, L. C., & Li, A. 2022, ApJ, 939, 22
Zhang, L., García-Bernete, I., Packham, C., et al. 2024, ApJ, 975, L2
Zhang, C., Hales, J., Peeters, E., et al. 2025, ApJS, 280, 4
Zubko, V., Dwek, E., & Arendt, R. G. 2004, ApJS, 152, 211

[1] Department of Physics and Astronomy, Universiteit Gent, Proeftuinstraat 86 N3, B-9000 Ghent, Belgium
[2] Institute of Astronomy, KU Leuven, Celestijnenlaan 200D, 3001 Leuven, Belgium
[3] Sorbonne Université, CNRS, UMR 7095, Institut d'Astrophysique de Paris, 98bis bd Arago, 75014 Paris, France
[4] Institut Universitaire de France, Ministère de l'Education Nationale, de l'Enseignement Supérieur et de la Recherche, 1 rue Descartes, 75231 Paris Cedex 05, France
[5] Centro de Astrobiología (CAB), CSIC-INTA, Camino Bajo del Castillo s/n, E-28692 Villanueva de la Cañada, Madrid, Spain
[6] Telespazio UK for the European Space Agency (ESA), ESAC, Camino Bajo del Castillo s/n, 28692 Villanueva de la Cañada, Spain
[7] European Space Agency, c/o Space Telescope Science Institute, 3700 San Martin Drive, Baltimore, MD 21218, USA
[8] UK Astronomy Technology Centre, Royal Observatory, Blackford Hill Edinburgh, EH9 3HJ Scotland, UK
[9] Observatorio Astronómico Nacional (OAN-IGN)-Observatorio de Madrid, Alfonso XII, 3, 28014, Madrid, Spain
[10] Leiden Observatory, Leiden University, PO Box 9513, 2300 RA Leiden, The Netherlands
[11] Dept. of Astrophysics, University of Vienna, Türkenschanzstr. 17, A-1180 Vienna, Austria
[12] ETH Zürich, Institute for Particle Physics and Astrophysics, Wolfgang-Pauli-Str. 27, 8093 Zürich, Switzerland
[13] Université Paris-Saclay, Université Paris Cité, CEA, CNRS, AIM, 91191 Gif-Sur-Yvette, France
[14] Department of Physics, University of Oxford, Keble Road, Oxford OX1 3RH, UK
[15] Department of Physics, University of California, San Diego, California 92093, USA
[16] Physikalisches Institut der Universität zu Kïln, Zülpicher Str. 77, D-50937, Köln, Germany; Max-Planck-Institut für Radioastronomie (MPIfR), Auf dem Hügel 69, D-53121 Bonn, Germany
[17] Department of Astronomy, Stockholm University, The Oskar Klein Centre, AlbaNova SE-106 91 Stockholm, Sweden
[18] LIRA, Observatoire de Paris, Université PSL, Sorbonne Université, Université Paris Cité, CY Cergy Paris Université, CNRS, 92190 Meudon, France
[19] Max Planck Institute for Astronomy, Königstuhl 17, 69117 Heidelberg, Germany
[20] Centre for Extragalactic Astronomy, Durham University, South Road, Durham DH1 3LE, UK

Table A.1. Setting for the mom0 extraction of H_2 0-0 S(1) emission line.

λ_{H2} [μm]	$\Delta\lambda_{H2}$ [μm]	$\Delta\lambda^{blue}_{cont}$ [μm]	$\Delta\lambda^{red}_{cont}$ [μm]
17.06	17.04 – 17.08	17.00 – 17.04	17.08 – 17.10

Notes. In the order we list: the observed central wavelength of the H_2 0-0 S(1) line (λ_{H2}), the wavelength interval used for its extraction ($\Delta\lambda_{H2}$), and the two continuum windows ($\Delta\lambda^{blue}_{cont}$, $\Delta\lambda^{red}_{cont}$).

Appendix A: Moment-0 maps of the most prominent PAH features

Figure A.1 shows the mom0 maps of the PAH bands at 6.2, 7.7, 8.6, 11.3, and 12.7 μm, while the 16.5 μm feature is displayed in the main text (Fig. 3). For completeness, we also include the mom0 map of the H_2 0-0 S(1) emission line. The latter was obtained through local continuum subtraction, following the prescriptions listed in Table A.1.

The PAH mom0 maps in Fig. A.1 exhibit a morphology consistent with that of the 16.5 μm PAH feature, with the exception of the 7.7 μm band, which instead appears to follow the H_2 distribution. We caution, however, that this behaviour may be influenced by residual contamination from the four emission lines blended with the 7.7 μm PAH complex (see Table 1).

Bright pixels near the AGN position are artifacts introduced by the local continuum subtraction and do not affect the PAH flux distribution at larger radii.

Appendix B: Regions for one-dimensional PAH extraction

We extracted 1D spectra over the wavelength range 4.9 – 21 μm from five regions of interest in the MIRI-MRS mosaic, described below.

(i) The full Ch 1A mosaic, spanning $7.2'' \times 3.6'' \sim 120 \times 60\,pc^2$, which allows comparison with studies of local Seyfert nuclei on scales of a few hundred parsecs.

(ii) The nucleus, treated as a point source and extracted using a conical aperture with a radius equal to twice the wavelength-dependent FWHM (Law et al. 2023):

$$\mathrm{FWHM}(\lambda) = 0.033'' \frac{\lambda}{\mu m} + 0.106'', \tag{B.1}$$

with FWHM = 0.35″ for $\lambda < 7$ μm and FWHM = 0.9″ for Ch 4A.

(iii) The circumnuclear region, that we obtained by subtracting the nuclear spectrum from that of the full Ch 1A mosaic.

(iv) The PAH ring, traced by the brightest pixels in the mom0 map of the 16.5 μm PAH feature (Fig. 3, left panel), i.e. with $S > 0.18 \times 10^{-14}\,erg\,cm^{-2}\,s^{-1}$.

(v) The PAH-deficient region, defined as the complement of the PAH ring area (excluding the nucleus). This region is spatially aligned with both the ionized-gas bubble identified by Alonso Herrero et al. (2025), which expands perpendicular to the jet, and the innermost inflowing branch of molecular gas traced by the CO(3–2) line (Espada et al. 2009). In addition, it shows the highest H_2/PAH ratio.

A schematic view of the regions for 1D PAH extraction is shown in the right panel of Fig. 3. All regions cover scales larger than the FWHM at 21 μm (∼ 0.9″), which ensures reliable spectral extraction and obviates the need to convolve to a common angular resolution.

Appendix C: On the extraction of PAH features in the nucleus

Between all the extraction regions, the nucleus yielded the poorest fit, with $\chi^2_{red} = 30$, and the largest residuals, especially across the 9 – 12 μm range. This suggests that the strong MIR continuum from the dusty AGN torus can significantly hinder a reliable extraction of the PAH features.

Our modelling framework includes PAH emission by default, which may not be appropriate for the nucleus, where the features do not clearly emerge above the continuum. In this appendix we assess the impact of excluding the PAH components from the spectral fit.

The resulting best-fit model without PAHs is shown in the bottom panel of Fig. C.1, together with the residuals. For comparison, the top panel reports the original fit obtained with the default configuration described in Sect. 3.2, which includes PAH components. Although both fits display residual structures with deviations of up to 8 – 10%, the reduced χ^2 is substantially lower when PAHs are included ($\chi^2_{red} = 30$ compared to $\chi^2_{red} = 102$ for the continuum-only model). An F-test indicated that the fit including the PAH features provides a statistically significant improvement over the alternative model, with a p-value $\ll 0.05$. This implies that some PAH emission is likely present even in the nucleus of Cen A; however, the strong MIR continuum prevents these features from being reliably constrained.

Appendix D: PAH modelling with CAFE

To assess the dependence of our results on the adopted spectral-decomposition method, we repeated the analysis using CAFE (Marshall et al. 2007; Diaz-Santos et al. 2025). This tool is widely employed in the literature to model the MIR spectra of starburst galaxies and AGNs (e.g. U et al. 2022; Lai et al. 2022, 2023; Armus et al. 2023; Bohn et al. 2024), and differs from SPIRIT primarily in its treatment of extinction. Other commonly used decomposition tools, such as PAHFIT (Smith et al. 2007; Van De Putte et al. 2025), are optimized, instead, for modelling emission from the diffuse ISM (e.g. Chastenet et al. 2026). We note that Maragkoudakis et al. (2025) reported differences of approximately 7% in the neutral PAH fraction when different spectral decomposition codes are employed.

As in SPIRIT, CAFE models PAH features with Drude profiles and allows variations in PAH central wavelength and width, though using fewer PAH subcomponents. Emission lines from warm molecular hydrogen and ionized gas are fitted with Gaussian profiles. The MIR continuum is described by: (i) dust re-emission, represented by cool, warm, and hot MBB components (initial temperatures $T = 75$, 135, 500 K) each with different opacity at 9.8 μm; (ii) direct continua, including a component mimicking the ISRF in the solar neighbourhood; starburst templates of age 2, 10, 100 Myr; and an AGN accretion-disc component, parameterized by multiple power laws. For modelling the integrated Cen A spectra, we adopted the default MIRI-AGN input parameter file.

Table D.1 lists the PAH feature intensities and associated uncertainties derived with CAFE, together with the fluxes of other relevant spectral lines. For reference, Table D.2 reports the PAH EWs, although we do not use them for our analysis. Figure D.1 shows the corresponding best-fit models and residuals. We find that the CAFE fits exhibit systematically larger

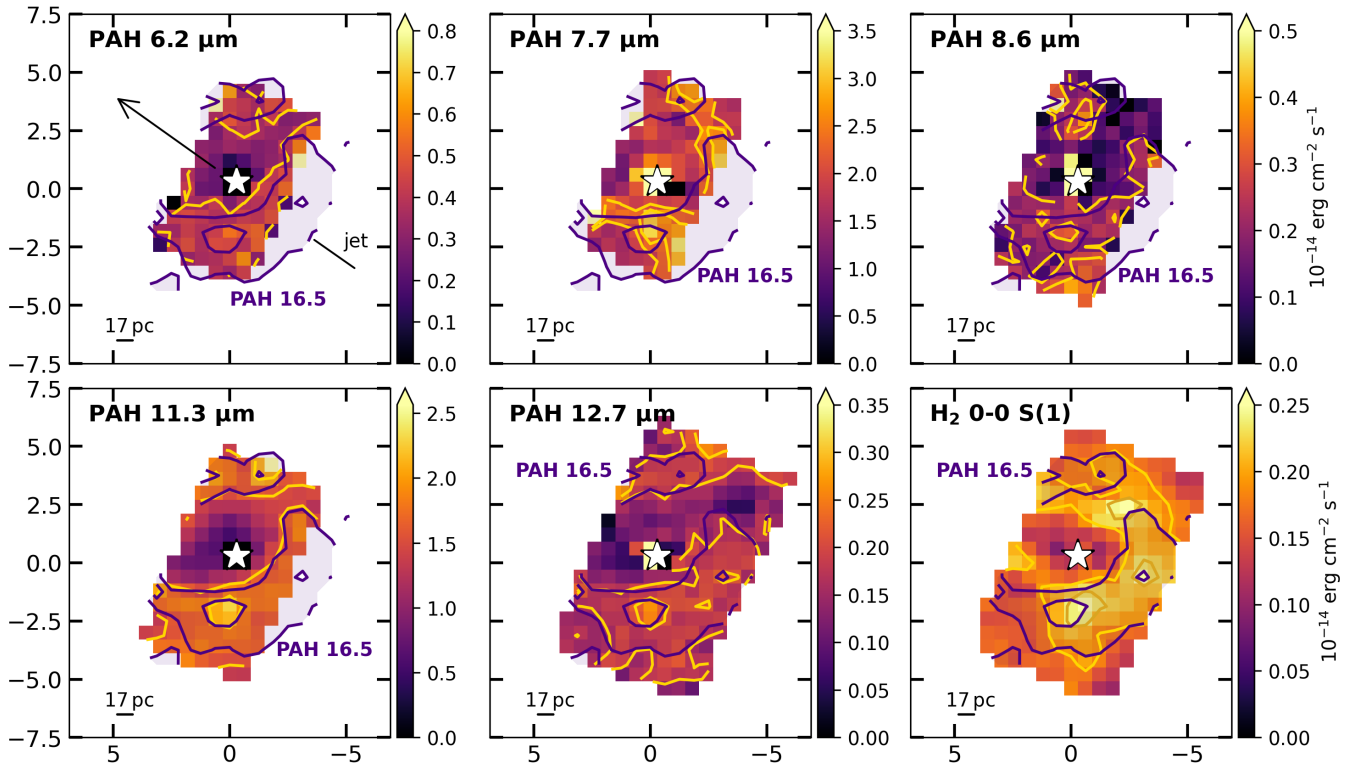

Fig. A.1. From top left to bottom right: mom0 maps of the most prominent PAH features (at 6.2, 7.7, 8.6, 11.3, and 12.7 µm) and the H_2 0-0 S(1) 17.03 µm line. We obtained the mom0 maps after subtraction of the local continuum, from the MIRI-MRS cube re-binned to spaxel scale of 0.6″ (Sect. 3.1). Yellow contours trace the feature emission at levels of: $[0.4, 0.55] \times 10^{-14}$ erg cm^{-2} s^{-1} (PAH 6.2); $[2, 2.75] \times 10^{-14}$ erg cm^{-2} s^{-1} (PAH 7.7); $[0.18, 0.27] \times 10^{-14}$ erg cm^{-2} s^{-1} (PAH 8.6); $[1.5, 2] \times 10^{-14}$ erg cm^{-2} s^{-1} (PAH 11.3); $[0.17, 0.22] \times 10^{-14}$ erg cm^{-2} s^{-1} (PAH 12.7); $[0.19, 0.23] \times 10^{-14}$ erg cm^{-2} s^{-1} (H_2 0-0 S(1)). Violet contours show the PAH 16.5 µm emission at $[0.18, 0.225] \times 10^{-14}$ erg cm^{-2} s^{-1}. In the top-left panel, the black arrow indicates the position angle of the jet (i.e. PA_{jet} = 51 deg). The stars correspond to the position of the AGN. North is up, and east is to the left.

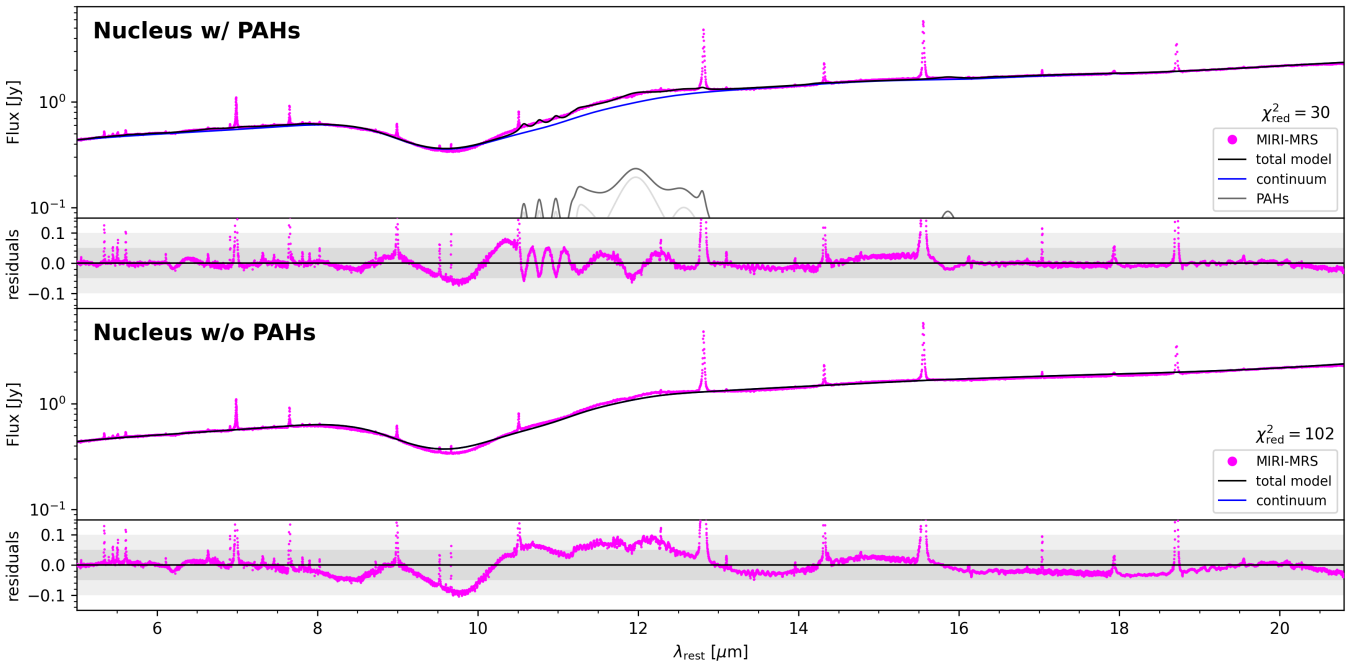

Fig. C.1. MIRI-MRS spectrum of Cen A's nucleus (magenta). The extraction region is shown in Appendix B. Black curves indicate the total best-fit models from the MIR decomposition tool (Donnan et al. 2024); the blue and grey curves show the fitted continua (stellar + AGN) and PAH components, respectively. Residuals are displayed beneath each panel, with the corresponding reduced χ^2 reported next to the legend. The top panel includes PAH features in the fit, while the bottom panel shows the fit obtained when PAH features are excluded.

Table D.1. PAH, warm molecular hydrogen, and ionized gas emission line intensities.

	[μm]	[10^{-17} W/m^2]	[10^{-17} W/m^2]	[10^{-17} W/m^2]	[10^{-17} W/m^2]	[10^{-17} W/m^2]
PAH	6.2	160 ± 140	41 ± 17	443 ± 130	68 ± 15	77 ± 29
PAH complex	7.7	370 ± 90	220 ± 20	1230 ± 280	210 ± 10	180 ± 40
PAH	8.61	44 ± 45	40 ± 10	500 ± 170	60 ± 5	80 ± 30
PAH complex	11.3	500 ± 50	225 ± 9	1600 ± 370	162 ± 6	235 ± 63
PAH	12	680 ± 70	750 ± 20	600 ± 180	58 ± 2	73 ± 25
PAH complex	12.7	560 ± 55	524 ± 16	650 ± 190	85 ± 3	90 ± 30
PAH complex	17	140 ± 40	67 ± 20	400 ± 120	70 ± 3	100 ± 30
H_2 0-0 S(3)	9.664	11 ± 2	–	90 ± 30	5.2 ± 0.4	19 ± 8
H_2 0-0 S(2)	12.279	8 ± 1	1.7 ± 0.5	26 ± 8	2.8 ± 0.1	6 ± 2
H_2 0-0 S(1)	17.035	12 ± 1	2.0 ± 0.5	44 ± 14	5.8 ± 0.2	11 ± 4
[Ne II]	12.814	69 ± 5	55 ± 2	70 ± 20	5.3 ± 0.2	9 ± 3
[Ne V]	14.3217	26 ± 3	22 ± 3	14 ± 5	0.9 ± 0.2	1.9 ± 0.6
[Ne III]	15.555	130 ± 10	118 ± 4	76 ± 23	7.2 ± 0.3	16 ± 5

Notes. Intensities are derived using CAFE. The second column lists the central wavelength of each feature. PAH complexes include the following subcomponents: 7.42, 7.60, 7.85 μm features (PAH 7.7); 11, 11.23 and 11.33 μm (PAH 11.3); 12.62 and 12.69 μm (PAH 12.7); and 16.45, 17.04, 17.375, and 17.87 μm (PAH 17).

Table D.2. PAH equivalent widths (EWs).

PAH λ_c [μm]	**Ch 1A mosaic** [nm]	**Nucleus** [nm]	**Circumnucl. reg.** [nm]	**PAH ring** [nm]	**PAH-def. reg.** [nm]
6.2	28	9	415	253	546
7.7 complex	100	76	1777	1185	1916
8.61	15	18	935	499	1134
11.3 complex	222	115	3847	1781	4834
12	276	364	1437	602	1395
12.7 complex	188	215	1448	796	1459
17 complex	61	41	1455	1036	2649

Notes. Same as Table D.1. Uncertainties are not available.

residuals than those obtained with SPIRIT (cf. Fig. 4). In particular, residuals reach up to ∼ 20% around 9.8 μm and in the vicinity of several PAH complexes, including the 6.2, 11.3, and 12.7 μm features. Moreover, approximately half of the PAH fluxes derived with CAFE are systematically higher by a factor of ∼ 2.

Appendix E: UV radiation field intensity in the centre of Cen A

UV radiation from the AGN accretion disc can efficiently excite PAH molecules within the central ∼ 500 pc (Jensen et al. 2017; Li 2020). In this appendix we estimate an upper limit to the UV radiation field illuminating the circumnuclear region of Cen A. The UV luminosity of an AGN can be approximated as

$$L_{\rm UV} = L_{\rm bol} - L_{2-10\,\rm keV}, \tag{E.1}$$

where the bolometric and X-ray luminosities are taken from Rothschild et al. (2011) and Beckmann et al. (2011). These values yield

$$L_{\rm UV} \simeq (10-3)\times 10^{42}\ \rm erg\ s^{-1} \approx 7\times 10^{42}\ \rm erg\ s^{-1}. \tag{E.2}$$

Since the PAH-emitting region lies at an average distance $R = 50$ pc ($\sim 1.54\times10^{18}$ m) from the central black hole, the corresponding UV flux is

$$F_{\rm UV} = \frac{L_{\rm UV}}{4\pi R^2} = \frac{7\times10^{42}}{4\pi\times(1.54\times10^{18})^2} \sim 2\times10^{5}\ \rm erg\ s^{-1}\ m^{-2}. \tag{E.3}$$

For comparison, the interstellar radiation field in the solar neighbourhood is ISRF = 2.2×10^{-5} W m^{-2} = 220 erg s^{-1} m^{-2} (Mathis et al. 1983; Galliano 2022). Hence, the radiation field impinging on the PAH ring in Cen A must be lower than ∼ 10^3 ISRF.

Appendix F: Neon fine structure line ratios and AGN models

Alonso Herrero et al. (2025), based on an analysis of fine-structure line intensity ratios, argued that the gas in the MIRI-MRS mosaic of Cen A is at least partially excited and ionized by shocks. In this appendix we compare the Neon fine-structure line ratios measured in the five regions analysed in this work (Appendix B) with the predictions of AGN radiative models and combined AGN+shock models (Feltre et al. 2023).

In Fig. F.1 we show the [Ne III]/[Ne II]×[Ne V]/[Ne II] diagnostic plot for the five region of interest. Their position on the plot is inconsistent with purely AGN radiative models, requiring a non-negligible contribution from shocks to excite the lines.

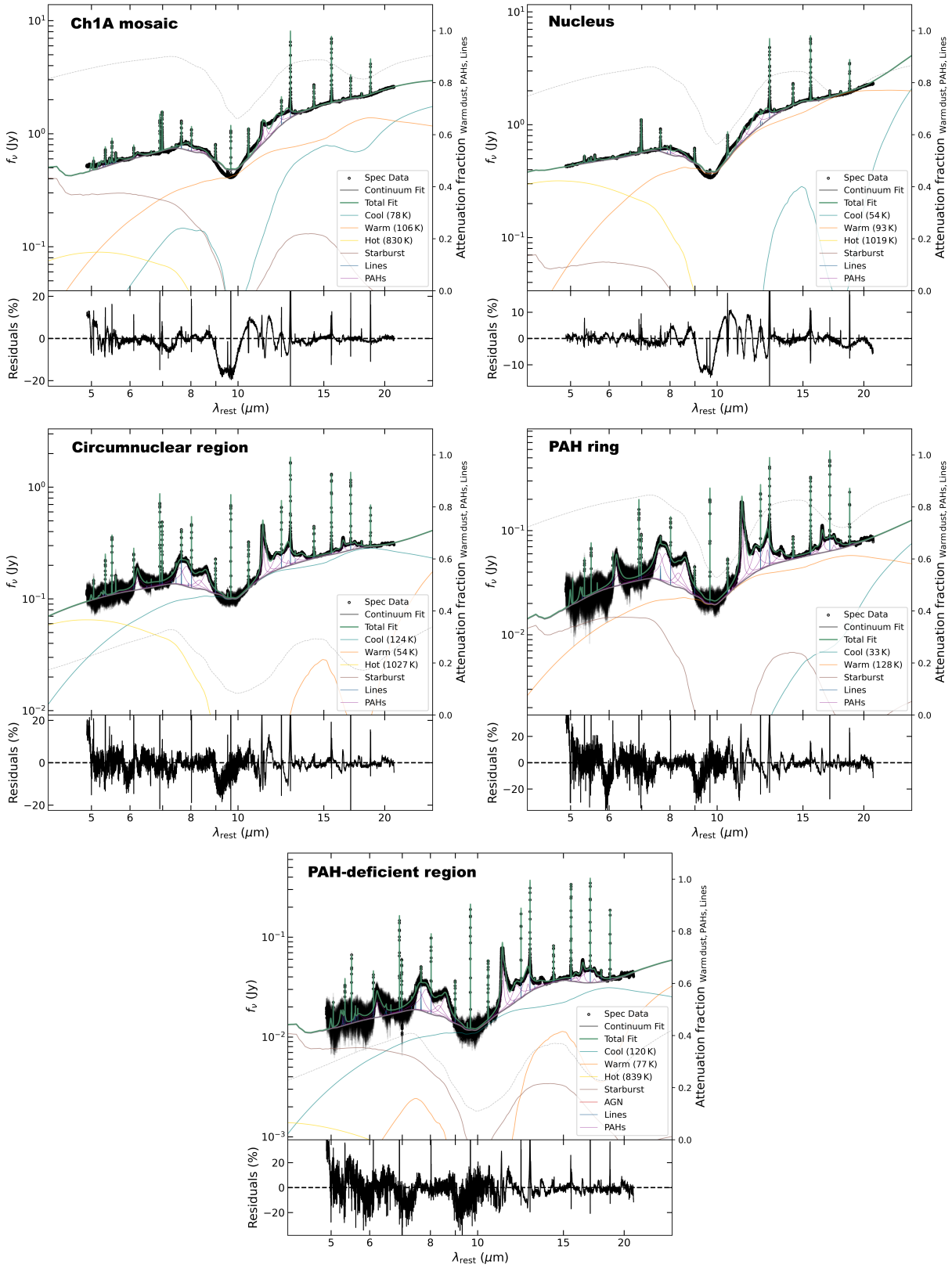

Fig. D.1. MIRI-MRS spectra extracted from the full Ch 1A mosaic, the nucleus, the circumnuclear region, the PAH ring, and the PAH-deficient region (see Appendix B), modelled with CAFE. The observed spectra are shown in black, the fitted continuum in grey, the PAH components in violet, and the total model in green. The continuum comprises a starburst component (brown) and cool, warm, and hot dust continua (light blue, orange, and yellow, respectively). The best-fit temperature of each component is indicated in brackets on the panels. The dashed gray line shows the dust attenuation. The lower insets display the residuals.

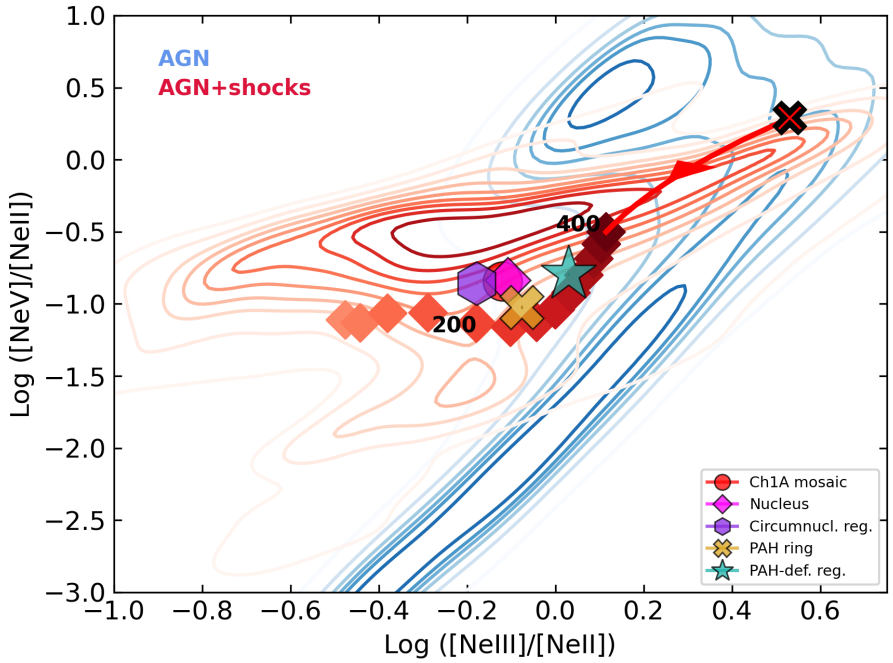

Fig. F.1. Neon line-ratio diagnostic diagram, showing $[\mathrm{Ne\,V}]_{14}$ / $[\mathrm{Ne\,II}]_{12}$ versus $[\mathrm{Ne\,III}]_{15}$ / $[\mathrm{Ne\,II}]_{12}$ for the five regions analysed: full Ch 1A mosaic (red circle), nucleus (magenta diamond), circumnuclear region (violet hexagon), PAH ring (yellow cross), and PAH-deficient region (green star). Blue density contours indicate the pure AGN models of Feltre et al. (2016), while red contours show the AGN+shock models of Feltre et al. (2023). The red arrow illustrates the effect of adding a 0 − 90% shock contribution to Hβ to an AGN model with $Z = 0.017$, $\log(\langle U \rangle) = -2.5$, $n_H = 103\,\mathrm{cm}^{-3}$, $\xi_d = 0.3$, and $\alpha = -1.7$ (black cross; Feltre et al. 2016). Orange diamonds mark AGN+shock models with a 90% shock contribution, with shock velocities increasing from 100 to 400 km s^{-1} (light to dark).